Immediate-foreshocks indicating a common cascading earthquake rupture development

Haoran Meng[1] and Wenyuan Fan[1]

[1]Scripps Institution of Oceanography, UCSD

November 23, 2022

Abstract

Understanding the seismic precursors is essential for deciphering earthquake rupture physics and can aid earthquake probabilistic forecasting. With regional dense seismic arrays, we identify seismic precursors of 527 0.9 [?] M [?] 5.4 events of the 2019 Ridgecrest earthquake sequence, including 48 earthquakes with series of precursors. These precursors are likely immediate-foreshocks that are adjacent to the earthquakes. Their corresponding precursory signals share high resemblances with the earthquake P-waves and occur within 100 s of the P-waves. However, attributes of the immediate-foreshocks, including the amplitudes and preceding times, do not clearly scale with the eventual earthquake magnitudes. Our observations suggest that earthquake rupture may initiate in a universal fashion but evolves stochastically. This indicates that earthquake rupture development is likely controlled by fine-scale fault heterogeneities in the Ridgecrest fault system, and the final magnitude is the only difference between small and large earthquakes.

Immediate-foreshocks indicating a common cascading earthquake rupture development

Haoran Meng[1] **and Wenyuan Fan**[1]

[1]Scripps Institution of Oceanography, UC San Diego, La Jolla, CA 92093-0225, USA

Key Points:

- Abundant immediate-foreshocks are observed for 527 Ridgecrest earthquakes.
- Characteristics of the precursory signals do not scale with the eventual earthquake magnitudes.
- These Ridgecrest earthquakes likely initiated as a rate-dependent cascading process.

Corresponding author: Haoran Meng, `h2meng@ucsd.edu`

Abstract

Understanding the seismic precursors is essential for deciphering earthquake rupture physics and can aid earthquake probabilistic forecasting. With regional dense seismic arrays, we identify seismic precursors of 527 $0.9 \leq M \leq 5.4$ events of the 2019 Ridgecrest earthquake sequence, including 48 earthquakes with series of precursors. These precursors are likely immediate-foreshocks that are adjacent to the earthquakes. Their corresponding precursory signals share high resemblances with the earthquake P-waves and occur within 100 s of the P-waves. However, attributes of the immediate-foreshocks, including the amplitudes and preceding times, do not clearly scale with the eventual earthquake magnitudes. Our observations suggest that earthquake rupture may initiate in a universal fashion but evolves stochastically. This indicates that earthquake rupture development is likely controlled by fine-scale fault heterogeneities in the Ridgecrest fault system, and the final magnitude is the only difference between small and large earthquakes.

Plain Language Summary

Earthquake precursory signals can inform earthquake initiation, and some precursors can generate seismic signals. Understanding such signals have both scientific and societal implications regarding earthquake physics and seismic hazards. Using dense arrays in the Ridgecrest region, we find abundant precursory signals of 527 earthquakes that occurred within a month of the 2019 M_w 7.1 Ridgecrest earthquake. These signals are likely generated by events that immediately slipped before the earthquakes within $\sim$1 km, hence immediate-foreshocks. Attributes of the precursory signal do not seem to correlate with the earthquake final magnitudes. Our observations suggest that earthquakes may initiate via similar means and it remains challenging to use such precursors to predict the their eventual magnitudes.

1 Introduction

Identifying and observing precursory signals of earthquakes have been of paramount importance because of their direct linkage with earthquake nucleation and rupture processes (e.g., Kanamori & Cipar, 1974; Ohnaka, 1992; Bouchon et al., 2013; Liu et al., 2020). Understanding such signals will offer insight of earthquake physics, but more importantly, knowledge of the signals can help hazard forecasting and mitigation (Mclaskey & Yamashita, 2017; Pritchard et al., 2020). The quest of short-term earthquake prediction has been paved with failed attempts, yet remains controversial (Kanamori, 2003; Sykes et al., 1999). This is because the observed precursory signals are often reported after the earthquakes and the examinations are not systematic, leaving the physical relations between these precursors and the mainshocks elusive. In practice, these signals are often difficult to identify without prior knowledge (Kanamori, 2003; Sykes et al., 1999). However, anomalous earthquake swarms and aseismic slips preceding the 2011 Tohoku-Oki and 2014 Iquique earthquakes show promising apparent precursors that can be observed to draw connections to the final megathrust ruptures (Kato et al., 2012; Ruiz et al., 2014). Yet, the consistency of such precursory signals is unclear, which hampers their practical implementations for operational warning purposes (Mignan, 2014, 2012).

Earthquake foreshocks are one key type of possible precursors and their spatiotemporal correlation with the mainshocks suggests that they may help describe the earthquake rupture preparation process (Kato et al., 2012; Ruiz et al., 2014; Trugman & Ross, 2019). However, the general prevalence of foreshocks is less clear and the physical origin of the foreshocks is not well understood (Abercrombie & Mori, 1996; Shearer & Lin, 2009; Ellsworth & Bulut, 2018; Tape et al., 2018; Seif et al., 2019; van den Ende & Ampuero, 2020; Moutote et al., 2020). Laboratory experiments have reported a range of precursors before earthquake-like lab-quakes (Marone, 1998; McLaskey & Lockner, 2014; Tinti et al., 2016; Bolton et al., 2019; Johnson et al., 2013; Goebel et al., 2013). For example, direct observations of multi-scale damage evolution in the failure zone (fault zone) suggest that there are fault nucleation and propagation processes, but the evolution depends on the fault stress/strength conditions, and can cause different precursors or precursors of different amplitudes for different fault systems (Renard et al., 2017, 2018). These experiments show similarities with the variability of foreshock occurrence and properties in nature (Chen & Shearer, 2013; Trugman & Ross, 2019). However, it is difficult to directly compare conventional foreshocks with laboratory experiments because of their vastly different spatiotemporal scales. Often, foreshocks are examined in a much larger spatiotemporal scale than that of the earthquake nucleation scale, leaving their relation with the mainshocks less clear.

Another type of precursors are termed nucleation phases (Spudich & Cranswick, 1984; Ellsworth & Beroza, 1995; McLaskey, 2019). Specifically, the nucleation phases are defined as accelerating aseismic slip events that are responsible for the following earthquakes (Ellsworth & Beroza, 1995; Beroza & Ellsworth, 1996; Lapusta & Rice, 2003; Kato et al., 2012; Ruiz et al., 2014). These nucleation phase investigations can be theorized as the pre-slip model (Ellsworth & Beroza, 1995; Dodge et al., 1996; McLaskey, 2019). In this model, earthquakes are nucleated by propagating aseismic slips and foreshocks are just by-products of the mainshock nucleation process. This implies that small and large earthquakes are initiated fundamentally differently and the aseismic slip size determines the nucleation length, which scales with the earthquake magnitude (Ellsworth & Beroza, 1995; Kato et al., 2012; Ruiz et al., 2014, 2017). Alternatively, numerous studies suggest that small and large earthquakes start the same way and it is difficult to predict the eventual earthquake magnitude or how the rupture would evolve based on the foreshocks or the P-wave onsets (Kilb et al., 2000; Uchide & Ide, 2010; Meier et al., 2017; Okuda & Ide, 2018; Ide, 2019; Yoon et al., 2019). These observations hint that small earthquakes can directly trigger other earthquakes by transferring stress on fault and eventually leading to the mainshock when the stress or strength condition is favorable for continuous rupture propagations, the cascade model (Ide & Aochi, 2005; McLaskey, 2019; Lui & Lapusta, 2016).

The clarity of the problem lies in robust observations of seismic precursors for earthquakes spanning a large range of magnitude but occurring in the same fault system. High-quality observations in such a relatively homogeneous geological environment are essential to track the effects of seismic precursors on the later stage ruptures. Specifically, understanding the earthquake nucleation process depends on knowing slip events shortly preceding the earthquakes, the immediate-foreshocks. We define immediate-foreshocks as slip events that can generate highly similar P-waves (precursory signals) as those of the mainshocks and are within a few folds of the mainshock rupture-dimension. We further require the immediate-foreshocks to occur within 100 seconds to ensure that the earthquakes are near-instantaneous responses of the immediate-foreshocks. In this study, we systematically investigate such immediate-foreshocks for 13,895 $0.5 \leq M \leq 5.4$ Ridgecrest earthquakes from 7 July 2019 to 6 August 2019 that were reported in Southern California Earthquake Data Center (SCEDC; Hutton et al., 2010). We find 527 earthquakes with clear precursory signals preceding P-waves generated by the immediate-foreshocks and these earthquakes are uniformly distributed across the whole fault system. These immediate-foreshocks suggest one type of common precursors preceding the Ridgecrest earthquakes, providing field observations that may bridge the conventional foreshocks and the laboratory precursors.

2 6 July 2019 M_w 5.4 Ridgecrest Earthquake

The 2019 Ridgecrest earthquake sequence, including a M_w 6.4 foreshock and a M_w 7.1 mainshock, provides an excellent opportunity to investigate the earthquake nucleation process (Figure 1a). The earthquake sequence was well recorded by regional broadband seismic networks and a number of rapid response campaign deployments soon after the foreshock on 4 July 2019 (Cochran et al., 2020; Ross et al., 2019). In particular, multiple three-component nodal arrays (deployed after 7 July 2019 for a month) enable investigations of moderate to small magnitude earthquakes in detail (Catchings et al., 2020). In total, 13,895 earthquakes with magnitudes (M) ranging from 0.5 to 5.4 have been detected and located for the sequence (SCEDC; Hutton et al., 2010) during the deployment of the nodal array. SCEDC uses a few different magnitude scales, including moment magnitudes for larger events and local magnitudes for smaller events. The rich dataset offers an ideal natural laboratory to examine the spatiotemporal evolution of a complete earthquake sequence at an unprecedented resolution (Cochran et al., 2020; Huang et al., 2020).

Located in between the foreshock and the mainshock, a 6 July 2019 M_w 5.4 earthquake has a clear immediate-foreshock (referred as E1 in Figures 1b, S1, and S2). The seismic records are band-pass filtered at 0.5 to 20.0 Hz with a causal 2nd-order Butterworth filter to avoid possible artifacts. There are signals arriving at stations 0.8 to 1.2 s prior to the P-wave, but they are 20 times smaller in amplitude on average. These signals share high resemblance with the P-waves, and the onsets of both phases can be fit by scaling the records of a M 3.7 earthquake that is 1.5 km away from the hypocenter (SCEDC catalog; Hutton et al., 2010). We further implement the records of the M 3.7 earthquake as empirical Green's functions (eGfs) to remove the path effects to obtain the apparent source time functions (ASTFs) of the M_w 5.4 earthquake for both P- and S-waves (McGuire, 2004; Fan & McGuire, 2018; Meng et al., 2020). The ASTFs show that there are at least two distinct subevents constituting the M_w 5.4 earthquake: the first subevent (E1) as the immediate-foreshock released about 4.8% of the total seismic moment (equivalent to a M_w 4.5 earthquake), while the second subevent (E2) occurred about 0.8 s later and released the remaining moment (Figure 1b and S2).

To test the robustness of the immediate-foreshock (subevent E1), we taper the ASTFs of E1 to zero (Figure S2a) and compute synthetic seismograms with only ASTFs of E2. The synthetics cannot explain the waveforms before the P-wave arrivals (Figure S2d), confirming the immediate-foreshock. The ASTFs also show that the earthquake ruptured towards the northeast direction and the centroid locations of the two subevents are 1.1 km apart (Figure S3). With a second moments analysis (McGuire, 2017; Meng et al., 2020, Text S1), we find that the subevent E2 likely ruptured 1.3 and 1.0 km along the strike and dip directions, respectively. We further compute the strain-tensor perturbations on the fault plane generated by E1 from the numerical spatial derivatives of the displacement field, with which we then use the Hooke's law to obtain the stress perturbations (Text S1). The subevent E2 is situated in a region where both static and dynamic stress perturbations from the immediate-foreshock exceed 0.1 MPa (Figure 1b), promoting an instantaneous slip event in the area (Figure S3). Our source model shows an evolving rupture process that the immediate-foreshock cascadingly nucleated the sequential stage rupture, E2, through a stress-triggering process. This confirms that E1 is a precursor of E2 and its seismic signals are precursory signals.

3 Abundant Immediate-foreshocks

To understand the prevalence of such nucleation process, we systematically investigate immediate-foreshocks of other earthquakes of the 2019 Ridgecrest sequence. We find that similar seismic precursory signals are a common feature of 527 Ridgecrest earthquakes, indicating abundant immediate-foreshocks (Figure 1a). For example, similar immediate-foreshocks are observed for a M 3.9 earthquake that is 2.7 km away from the M_w 5.4 event, and the P waveforms of the M 3.9 earthquake are almost identical to the P-wave onsets of the M_w 5.4 subevents (Figure 2). Further, clear immediate-foreshocks can be identified for earthquakes as small as M 0.9 (Figure 2). We observe abundant yet diverse immediate-foreshocks of earthquakes spanning five magnitudes in a single 40-km-long fault system (Figures 1a and 3).

We identify these precursory signals by autocorrelating 0.5 to 1.0 s long P-waves with waveforms that precede the P-waves by 100 s. The autocorrelation is independently performed for all stations within 30 km of the event epicenter (Text S2). For example, a precursory signal (indicating an immediate-foreshock) is detected for a $M \leq 3.5$ earthquake when the average autocorrelation coefficient exceeds 0.8 for more than 10 stations and these stations are from a minimum azimuthal range of 180°. For a detected immediate-foreshock, we document the amplitude ratios and the preceding times (differential time from the autocorrelation procedure) between the precursory signals and the P-waves (Figure 2 and see Text S2). The immediate-foreshock is further examined by requiring the measured preceding time distribution to have a standard deviation that is less than 0.01 s for $M \leq 3.5$ earthquakes (Text S2). This quality control procedure assures that the immediate-foreshocks generating the precursory signals are adjacent to their mainshocks and they share the same focal mechanism, although the rupture details remain unresolved due to the data limitation. Finally, our procedure rules out the possibility of the detected precursory signals as the fault zone head waves because of a lack of systematic phase moveouts for sensors across the fault zone (Figures S4 and S5) (Ben-Zion & Malin, 1991; Ben-Zion et al., 1992).

In total, we examine 13,895 $0.5 \leq M \leq 5.4$ earthquakes in the Ridgecrest region that are reported in the SCEDC catalog (Hutton et al., 2010) and find that 527 events with immediate-foreshocks can be robustly identified (Table S1), out of which the M_w 5.4 earthquake preceded the M_w 7.1 earthquake while the remaining events were aftershocks of the M_w 7.1 earthquake. The lack of events with immediate-foreshocks prior to the M_w 7.1 earthquake (6 July 2019) is likely due to a data deficiency as the nodal arrays on the fault zone were only deployed after 7 July 2019 (Catchings et al., 2020). Our analysis relies on the near-fault dataset and an autocorrelation method to study the earthquake preparation process. Therefore, we do not analyze the M_w 6.4 or M_w 7.1 earthquakes as the autocorrelation procedure is less effective for these large earthquakes, which would require other approaches for detailed analyses (e.g. Ellsworth & Bulut, 2018; Yoon et al., 2019).

We observe immediate-foreshocks of earthquakes with magnitudes ranging from 0.9 to 5.4 and find these earthquakes have a similar magnitude-frequency distribution to that of the 13,895 investigated earthquakes (Figure S6). Additionally, the immediate-foreshocks do not show characteristics that can differentiate the mainshocks of different fault segments (Figure 1a). These 527 earthquakes are distributed across the whole seismogenic zone from 0 to 13 km, penetrating beyond the creeping transition depth at 11.0 km (Figure 3g and see Text S3). The immediate-foreshocks generate precursory signals preceding the mainshock P-waves by 0.5 to 100 s. These preceding times do not seem to scale with earthquake magnitudes nor depths (Figures 3b and h). Intriguingly, amplitude ratios of $M \geq 2.5$ events are larger on average than those of smaller magnitude earthquakes (Figure 1a and Figure S6c). However, the robustness of this observation is difficult to verify due to fewer $M \geq 2.5$ earthquakes (total 41 events). These $M \geq 2.5$ earthquakes are more likely to have higher amplitude ratios for the same noise level and detection threshold (detecting more low-amplitude precursory signals) because low amplitude precursory signals of smaller earthquake are more likely buried in the background noise than those of larger events.

Using the differential times obtained from the autocorrelation procedure and a 1D average velocity model of Southern California (Lee et al., 2014), we further determine the relative locations between the 527 earthquakes and their immediate-foreshocks (Figure 4a and see Text S4). About 84% of these immediate-foreshocks are located within 0.2 km of the mainshock hypocenters with a median separation of 59 m (Figure 4a). We further evaluate the relative location uncertainty by performing jackknife-resampling of the stations (Efron & Tibshirani, 1994) (Text S4). About 85% of the separation distance between the immediate-foreshocks and mainshocks has a standard deviation less than

0.1 km with a median value of 15 m horizontally (Figure S7f). Vertically, 78% of the separation distance has a standard deviation less than 0.1 km with a median value of 31 m (Figure S7f). Further, we observe more than 85% of the immediate-foreshocks occurred within 60 s of the mainshocks despite the searching window is 100 s long (Figure 4c). Without knowing the magnitudes and stress-drop estimates of the immediate-foreshocks, we cannot evaluate the static/dynamic stress perturbations at the mainshock locations from the immediate-foreshocks. However, the spatiotemporal clustering suggests that the immediate-foreshocks likely near-instantaneously triggered the following slip, indicating a rapid rupture development (Shearer & Lin, 2009; Yoon et al., 2019).

Out of the 527 earthquakes, 48 earthquakes have series of successive precursory signals, indicating a possible complex evolution of the rupture developments. For example, we identify two immediate-foreshocks for a M 2.5 earthquake (Figures 2 and S5). This sequence of precursory signals share high resemblances with the M 2.5 earthquake P-waves with an average cross-correlation coefficient of 0.91, yet their amplitudes are 127.6 and 1067.8 times smaller than the P-waves on average (Figure S5). These observations likely represent a hierarchical nucleation process that the observed earthquakes are products of a series of cascadingly triggered slip patches (Wyss & Brune, 1967; Fukao & Furumoto, 1985; Ide, 2019; Okuda & Ide, 2018; Ellsworth & Bulut, 2018; Abercrombie & Mori, 1994). These observations also suggest that the Ridgecrest fault system may have a fractal strength or stress structure over orders of scale. Characteristics of these 48 earthquakes and their immediate-foreshocks, including the earthquake location, amplitude ratio, and preceding time, show no differences to those of the rest 479 earthquakes that only have single precursors, rendering that earthquake rupture development is stochastic and local fine-scale heterogeneous fault properties control the rupture evolution (Ide, 2019; McLaskey, 2019; Ide & Aochi, 2005).

4 Discussions and Conclusions

The observed immediate-foreshocks show clear spatiotemporal correlations with the following earthquakes (Figures 4a and 4b), but are they precursors of the earthquakes or simply random forerunners? To evaluate the influence of the immediate-foreshocks in nucleating the following slip, we compare the immediate-foreshocks with cataloged earthquakes in Shelly (2020). We first investigate the spatiotemporal behaviors of all the cataloged earthquakes that are within 1 km to the 527 earthquake hypocenters, which have one or more immediate-foreshocks. The separation distance and time between two sequential cataloged earthquakes show different distributions comparing to those of the immediate-foreshocks (Figures 4c and 4d). These sequential earthquakes seem to be relatively uniformly separated in space (within 1 km), and the separation time seems to be Poissonian. Such characteristics show that the sequential earthquakes are mostly independent, random cases. In contrast, the immediate-foreshocks cluster in space and time, suggesting they are not random but more likely have influenced the following earthquakes, hence precursors.

We also compare the immediate-foreshocks with correlated seismicity in Shelly (2020), including foreshock-mainshock and mainshock-aftershock sequences (Figure S8). These sequences are defined as sequential earthquakes occurring within 1 km and 100 s and the foreshocks/aftershocks having smaller magnitudes comparing to the mainshocks (across the whole region, not just near the 527 earthquakes with immediate-foreshocks). In Shelly (2020), there are 363 foreshock-mainshock and 519 mainshock-aftershock sequences (Text S5). The separation distances between the foreshocks/aftershocks and the mainshocks show similarities with the immediate-foreshocks as they all cluster within 0.2 km of the mainshock hypocenters (Figure 4d). The separation time distributions are different (Figure 4c). There seems to be an apparent paucity of aftershocks soon after the mainshocks and most of the aftershocks seem to occur at or after 20 s of the mainshocks. The lack of aftershocks soon after the mainshocks may be due to the coda waves or noises in the records

(Kagan & Houston, 2005). The foreshocks in the high resolution catalog are akin to the immediate-foreshocks, i.e., clustering spaiotemporally with the mainshocks, but also show differences. Most of the foreshocks occurred more than 5 s ahead of the mainshocks, while our immeidate-foreshocks peak within 5 s of the following mainshocks (Figure 4b,c). Further, the occurrence of the 527 observed immediate-foreshocks and the 363 foreshocks in Shelly (2020) follow the inverse Omori's law as there are more immediate-foreshocks and catalog foreshocks as the the mainshocks approach, but the two classes of seismicity grow at different rates (Figure S9 and see Text S6).

In most studies, the term "foreshock" is loosely defined, and they are often considered in a much larger spatiotemporal scales, i.e., over ten of kilometers and/or days of periods (Abercrombie & Mori, 1996; Shearer & Lin, 2009; Chen & Shearer, 2013; Trugman & Ross, 2019). The foreshocks that we search in the high resolution catalog (Shelly, 2020) are specific events analogous to our immediate-foreshocks, and they are selected based on strict constraints in space and time (Figure 4). Therefore, the observed variations of the foreshocks and immediate-foreshocks in Figure 4c may not be inconsistent but represent the same process at two resolutions. For example, characteristics of these foreshock-mainshock sequences show similar patterns as those of the observed immediate-foreshocks, and we do not find clear scaling relationships among the earthquake magnitude, depth, preceding time, and magnitude difference (Figure S8). Therefore, the foreshocks in the high resolution catalog (Shelly, 2020) and the immediate-foreshocks in this study may demonstrate the same type of preparation phase for the mainshocks. Particularly, our immediate-foreshocks offer a high resolution view of slip events ahead of the earthquake onsets because of the spatial collocation and the short separation time. They demonstrate a near-instantaneous response of the following slip events, indicating that the mainshocks are nucleated by stress transferring from the immediate-foreshocks.

The current set of observations can be best explained by the cascade model (Wyss & Brune, 1967; Fukao & Furumoto, 1985; Ide & Aochi, 2005; Aochi & Ide, 2004; Lui & Lapusta, 2016). In this cascade model, a slip event on a small fault patch that is adjacent or within the earthquake rupture area rapidly transfers stress to a surrounding fault and leads to an unsteady dynamic rupture (Ide & Aochi, 2005; Lui & Lapusta, 2016; McLaskey, 2019). Such processes have been observed in earthquakes with a range of magnitudes. For example, the 1964 Mw 9.2 Alaska earthquakes was shortly preceded by a sequence of earthquakes within 100 s (likely immediate-foreshocks) before its onset, and the propagating rupture of the sequence eventually led to the great earthquake (Wyss & Brune, 1967). The propagation of such a cascade process is controlled by the local stress and strength heterogeneities, which effectively reflect as hierarchically distributed fault patches, and naturally, the barriers between such patches determine the termination of the cascade process, the earthquake eventual magnitude (Fukao & Furumoto, 1985; Noda et al., 2013; Aochi & Ide, 2004; Ide & Aochi, 2005). It is worth noting that large earthquakes (e.g., M$\geq$6) have P-waves significantly different from those of small events, therefore, we did not investigate the M_w 6.4 and the M_w 7.1 Ridgecrest earthquakes. However, foreshocks seem to have cascadingly triggered the M_w 6.4 earthquake without evidence of observable aseismic slips (Ellsworth et al., 2020).

The structure of hierarchical fault patches implies multiscale heterogeneities, which is likely the physical cause of the series of successive precursory signals (Figures 2 and S5). These fault patches and heterogeneities associate with the stress distribution, fault roughness, and fault gouge, which may have developed naturally as the fault structure evolves over multiple seismic cycles (Davidesko et al., 2014; Martel et al., 1988; Trugman et al., 2020). In particular, the 2019 Mw 7.1 Ridgecrest earthquake has caused stress variabilities on length scales of hundreds of meters or less, leading to faulting complexities throughout the earthquake sequence (Trugman et al., 2020). Such complex structures and heterogeneities have scales comparable to those of the separation distances between the immediate-foreshocks and the mainshocks (Figure 4), favoring the cascade nucleation process. Previous numerical studies show that the rate-and-state friction law and a set of randomly distributed fractal fault patches can produce a wide variety of cascading rupture scenarios for both small and large earthquakes (Fukao & Furumoto, 1985; Ide, 2019). Furthermore, recent laboratory experiments suggest a rate-dependent cascade process that may have been facilitated by the varying nucleation length in addition to the fault property heterogeneities (McLaskey, 2019). These studies suggest that the final magnitude is the only difference between small and large earthquakes. For the Ridgecrest earthquakes, the lack of scaling relations between the precursory signals and the P-waves and the diverse characteristics of the immediate-foreshocks indicate such a stochastic rupture development and support the cascade model (Figure 3). Our results concur that earthquakes nucleate in a similar fashion and large events are simply results of favorable continuous rupture conditions. For example, the M 3.9 and the M_w 5.4 earthquakes occurred within 2.6 km and have similar precursory signals (SCEDC; Hutton et al., 2010), but the final moments were 165 times different (Figures 2, S1–2, and S4). Such disparities emphasize that fine-scale heterogeneities or barriers modulate earthquake rupture development in complex ways.

Another possible nucleation mechanism is the preslip model (Ellsworth & Beroza, 1995; McLaskey, 2019; Dodge et al., 1996). In this model, the final earthquake magnitude correlates with the aseismic slip size, which can trigger foreshocks but the foreshocks do not prepare the following mainshocks. Therefore, this model hints that the aseismic nucleation characteristics would affect the later stage rupture of an earthquake, although seismic observations of the preslip model may be indistinguishable from those caused by the cascade model (Ellsworth & Beroza, 1995). Recent observations of some large subduction zone earthquakes can be explained by this model (Kato et al., 2012; Ruiz et al., 2014, 2017). The preslip model would suggest that earthquake nucleation preferentially occurs at the transition zones between the creeping and locked fault segments and a coalescence of seismicity would migrate around the earthquake epicenter for some extended period before the fault slip reaching a critical nucleation length (Lapusta & Rice, 2003; Tape et al., 2018). In our observations, earthquakes with immediate-foreshocks occurred at all depths beyond the transition zone, and we rarely observe more than one precursory signals for a given earthquake. However, additional precursory signals may have been missed by our autocorrelation procedure, which is less effective at detecting aseismic slips or slip events that are away from the earthquake hypocenter. It is possible that multiple processes have occurred concurrently and have modulated the nucleation process as a rate-dependent feedback system, which has been documented in experiments, simulations, and field observations (McLaskey, 2019; Lapusta & Rice, 2003; Yao et al., 2020).

We do not observe seismic precursory signals for every investigated earthquake. Roughly, 4% of the 13,895 earthquakes have identifiable immediate-foreshocks. This is likely limited by the data as the majority of the immediate-foreshocks are inferred from the nodal array data, and the precursory signals are often buried in noise at the regional network stations. It is also possible that there are more immediate-foreshocks but their separation times are too short to be resolved by our current procedure or available data. Additionally, our procedure may have excluded seismic precursory signals beyond the 100 s time window that we have scanned through. In this case, there might be other preparation processes than the near-instantaneous stress transferring nucleation as demonstrated by the immediate-foreshocks. Finally, our observations only represent one class of the earthquake nucleation processes and there are other physical mechanisms initiating the Ridgecrest earthquakes in addition to the aforementioned end-member models. Nevertheless, the immediate-foreshocks highlights the importance of near-field observations, in particular, the needs of fault-zone observations.

Whether the growth trajectory of an earthquake can be robustly forecasted depends on understanding the influences of the earthquake precursors over the later stage rupture (Meier et al., 2017; McLaskey, 2019; Mori & Kanamori, 1996; Iio, 1992). Fine-scale rate-dependent physical processes, e.g., grain crushing, microcracking, and plastic deformation, may have strong impacts on the earthquake rupture development (Yamashita, 2000; Xu et al., 2019). Such processes are challenging to measure geophysically and cannot be deterministically predicted, which may cause small and large earthquakes showing similar seismic precursors.

For the Ridgecrest earthquakes, we find abundant immediate-foreshocks for earthquakes with magnitude from 0.9 to 5.4 that may have helped nucleating the earthquakes. Numerous earthquakes occurred in the same region showing similar seismic precursory signals but developed into events with different eventual magnitudes, illuminating the limited predictability of the earthquake growth process (Figure 3). For instance, we find that there is no scaling relationship between the amplitude ratio or the preceding time with the earthquake magnitude (Figures 3a and b). However, we find that all the observed immediate-foreshocks occurred within 100 s of the earthquakes with a temporal clustering around 7 seconds and 0.06 km (Figure S10). This time-distance clustering of the 527 earthquakes and their immediate-foreshocks shows a possible common preparation process that nucleate earthquakes near-instantaneously in the Ridgecrest fault system.

Data Availability Statement

The 13,895 earthquakes investigated in the study are from the Southern California Earthquake Data Center catalog (SCEDC; Hutton et al., 2010). The high resolution catalog used for comparision is from Shelly (2020). The seismic records were provided by Data Management Center (DMC) of the Incorporated Research Institutions for Seismology (IRIS) and the SCEDC (Caltech.Dataset., 2013). The nodal array data is openly available through IRIS DMC and was acquired by the U.S. Geological Survey (USGS) (Catchings et al., 2020), the Southern California Earthquake Center (SCEC), and SCEC member institutions. The 1D velocity model used in this study is obtained from averaging the community velocity model of Southern California (Lee et al., 2014). The earthquakes that have immediate-foreshocks are listed in Table S1.

Acknowledgments

The research was supported by NSF EAR-2022441 and by the Southern California Earthquake Center (SCEC; Award No. 20115 and Contribution No. 10957). SCEC is funded by NSF Cooperative Agreement EAR-1600087 & USGS Cooperative Agreement G17AC00047. We thank the editor Dr. Prieto, AE Dr. Tsai, Dr. Trugman, an anonymous reviewer, Dr. Shearer, Dr. Barbour, and Dr. McGuire for their insightful, constructive suggestions, which have led to improvements in the paper.

References

Abercrombie, R. E., & Mori, J. (1994). Local observations of the onset of a large earthquake: 28 June 1992 Landers, California. *Bulletin of the Seismological Society of America*, *84*(3), 725–734.

Abercrombie, R. E., & Mori, J. (1996). Occurrence patterns of foreshocks to large earthquakes in the western united states. *Nature*, *381*(6580), 303–307.

Aochi, H., & Ide, S. (2004). Numerical study on multi-scaling earthquake rupture. *Geophysical research letters*, *31*(2).

Ben-Zion, Y., Katz, S., & Leary, P. (1992). Joint inversion of fault zone head waves and direct P arrivals for crustal structure near major faults. *Journal of Geophysical Research: Solid Earth*, *97*(B2), 1943–1951.

Ben-Zion, Y., & Malin, P. (1991). San Andreas fault zone head waves near Parkfield, California. *Science*, *251*(5001), 1592–1594.

Beroza, G. C., & Ellsworth, W. L. (1996). Properties of the seismic nucleation phase. *Tectonophysics*, *261*(1-3), 209–227.

Bolton, D. C., Shokouhi, P., Rouet-Leduc, B., Hulbert, C., Rivière, J., Marone, C., & Johnson, P. A. (2019). Characterizing acoustic signals and searching for precursors during the laboratory seismic cycle using unsupervised machine learning. *Seismological Research Letters*, *90*(3), 1088–1098.

Bouchon, M., Durand, V., Marsan, D., Karabulut, H., & Schmittbuhl, J. (2013). The long precursory phase of most large interplate earthquakes. *Nature Geoscience*, *6*(4), 299–302. doi: 10.1038/ngeo1770

Caltech.Dataset. (2013). Southern California Earthquake Data Center. doi: 10.7909/C3WD3xH1

Catchings, R. D., Goldman, M., Steidl, J., Chan, J., Allam, A., Criley, C., ... Ben-Zion, Y. (2020). Nodal seismograph recordings of the 2019 Ridgecrest earthquake sequence. *Seismological Research Letters*, *91*(6), 3622—3633.

Chen, X., & Shearer, P. M. (2013). California foreshock sequences suggest aseismic triggering process. *Geophysical Research Letters*, *40*(11), 2602–2607.

Cochran, E. S., Wolin, E., McNamara, D. E., Yong, A., Wilson, D., Alvarez, M., ... Steidl, J. (2020). The U.S. Geological Survey's rapid seismic array deployment for the 2019 Ridgecrest Earthquake Sequence. *Seismological Research Letters*, *91*(4), 1952–1960. doi: 10.1785/0220190296

Davidesko, G., Sagy, A., & Hatzor, Y. H. (2014). Evolution of slip surface roughness through shear. *Geophysical Research Letters*, *41*(5), 1492–1498.

Dodge, D. A., Beroza, G. C., & Ellsworth, W. L. (1996). Detailed observations of california foreshock sequences: Implications for the earthquake initiation process. *Journal of Geophysical Research: Solid Earth*, *101*(B10), 22371–22392.

Efron, B., & Tibshirani, R. J. (1994). *An introduction to the bootstrap*. CRC press.

Ellsworth, W. L., Barbour, A. J., & Shelly, D. R. (2020). Foreshock cascade to failure in the m_w 6.4 July 4, 2019 Ridgecrest, California earthquake. *Poster Presentation at 2020 SCEC Annual Meeting*.

Ellsworth, W. L., & Beroza, G. (1995). Seismic evidence for an earthquake nucleation phase. *Science*, *268*(5212), 851–855.

Ellsworth, W. L., & Bulut, F. (2018). Nucleation of the 1999 Izmit earthquake by a triggered cascade of foreshocks. *Nature Geoscience*, *11*(7), 531–535.

Fan, W., & McGuire, J. J. (2018). Investigating microearthquake finite source attributes with IRIS community wavefield demonstration experiment in Oklahoma. *Geophysical Journal International*, *214*(2), 1072–1087.

Fukao, Y., & Furumoto, M. (1985). Hierarchy in earthquake size distribution. *Physics of the earth and planetary interiors*, *37*(2-3), 149–168.

Goebel, T., Schorlemmer, D., Becker, T., Dresen, G., & Sammis, C. (2013). Acoustic emissions document stress changes over many seismic cycles in stick-slip experiments. *Geophysical Research Letters*, *40*(10), 2049–2054.

Huang, H., Meng, L., Bürgmann, R., Wang, W., & Wang, K. (2020). Spatiotemporal foreshock evolution of the 2019 M 6.4 and M 7.1 Ridgecrest, California earthquakes. *Earth and Planetary Science Letters*, *551*, 116582.

Hutton, K., Woessner, J., & Hauksson, E. (2010). Earthquake monitoring in southern California for seventy-seven years (1932–2008). *Bulletin of the Seismological Society of America*, *100*(2), 423–446.

Ide, S. (2019). Frequent observations of identical onsets of large and small earthquakes. *Nature*, *573*(7772), 112–116.

Ide, S., & Aochi, H. (2005). Earthquakes as multiscale dynamic ruptures with heterogeneous fracture surface energy. *Journal of Geophysical Research: Solid Earth*, *110*(B11).

Iio, Y. (1992). Slow initial phase of the P-wave velocity pulse generated by microearthquakes. *Geophysical research letters*, *19*(5), 477–480.

Jin, Z., & Fialko, Y. (2020). Finite slip models of the 2019 Ridgecrest earthquake sequence constrained by space geodetic data and aftershock locations. *Bulletin of the Seismological Society of America*, *110*(4), 1660–1679.

Johnson, P. A., Ferdowsi, B., Kaproth, B. M., Scuderi, M., Griffa, M., Carmeliet, J., ... Marone, C. (2013). Acoustic emission and microslip precursors to stick-slip failure in sheared granular material. *Geophysical Research Letters*, *40*(21), 5627–5631.

Kagan, Y. Y., & Houston, H. (2005). Relation between mainshock rupture process and omori's law for aftershock moment release rate. *Geophysical Journal International*, *163*(3), 1039–1048.

Kanamori, H. (2003). Earthquake prediction: an overview. *International Geophysics*, *81*(PART B), 1205–1216. doi: 10.1016/S0074-6142(03)80186-9

Kanamori, H., & Cipar, J. J. (1974). Focal process of the great Chilean earthquake May 22, 1960. *Physics of the Earth and Planetary Interiors*, *9*(2), 128–136. doi: 10.1016/0031-9201(74)90029-6

Kato, A., Obara, K., Igarashi, T., Tsuruoka, H., Nakagawa, S., & Hirata, N. (2012). Propagation of slow slip leading up to the 2011 Mw 9.0 Tohoku-Oki earthquake. *Science*, *335*(6069), 705–708. doi: 10.1126/science.1215141

Kilb, D., Gomberg, J., & Bodin, P. (2000). Triggering of earthquake aftershocks by dynamic stresses. *Nature*, *408*(6812), 570–574.

Lapusta, N., & Rice, J. R. (2003). Nucleation and early seismic propagation of small and large events in a crustal earthquake model. *Journal of Geophysical Research: Solid Earth*, *108*(B4).

Lee, E.-J., Chen, P., Jordan, T. H., Maechling, P. B., Denolle, M. A., & Beroza, G. C. (2014). Full-3-D tomography for crustal structure in southern California based on the scattering-integral and the adjoint-wavefield methods. *Journal of Geophysical Research: Solid Earth*, *119*(8), 6421–6451.

Liu, Y., McGuire, J. J., & Behn, M. D. (2020). Aseismic transient slip on the Gofar transform fault, East Pacific Rise. *Proceedings of the National Academy of Sciences*, *117*(19), 10188–10194.

Lui, S. K., & Lapusta, N. (2016). Repeating microearthquake sequences interact predominantly through postseismic slip. *Nature communications*, *7*(1), 1–7.

Marone, C. (1998). Laboratory-derived friction laws and their application to seismic faulting. *Annual Review of Earth and Planetary Sciences*, *26*(1), 643–696.

Martel, S. J., Pollard, D. D., & Segall, P. (1988). Development of simple strike-slip fault zones, Mount Abbot quadrangle, Sierra Nevada, California. *Geological Society of America Bulletin*, *100*(9), 1451–1465.

McGuire, J. J. (2004). Estimating finite source properties of small earthquake ruptures. *Bulletin of the Seismological Society of America*, *94*(2), 377–393. doi: 10.1785/0120030091

McGuire, J. J. (2017). A MATLAB toolbox for estimating the second moments of earthquake ruptures. *Seismological Research Letters*, *88*(2A), 371–378. doi: 10.1785/0220160170

McLaskey, G. C. (2019). Earthquake initiation from laboratory observations and implications for foreshocks. *Journal of Geophysical Research: Solid Earth*, *124*(12), 12882–12904.

McLaskey, G. C., & Lockner, D. A. (2014). Preslip and cascade processes initiating laboratory stick slip. *Journal of Geophysical Research: Solid Earth*, *119*(8), 6323–6336.

Mclaskey, G. C., & Yamashita, F. (2017). Slow and fast ruptures on a laboratory fault controlled by loading characteristics. *Journal of Geophysical Research: Solid Earth*, *122*(5), 3719–3738.

Meier, M.-A., Ampuero, J., & Heaton, T. H. (2017). The hidden simplicity of subduction megathrust earthquakes. *Science*, *357*(6357), 1277–1281.

Meng, H., McGuire, J. J., & Ben-Zion, Y. (2020). Semiautomated estimates of directivity and related source properties of small to moderate southern California earthquakes using second seismic moments. *Journal of Geophysical Research: Solid Earth*, *125*(4), e2019JB018566.

Mignan, A. (2012). Seismicity precursors to large earthquakes unified in a stress accumulation framework. *Geophysical Research Letters*, *39*(21), 1–5. doi: 10.1029/2012GL053946
Mignan, A. (2014). The debate on the prognostic value of earthquake foreshocks: a meta-analysis. *Scientific reports*, *4*, 4099.
Mori, J., & Kanamori, H. (1996). Initial rupture of earthquakes in the 1995 Ridgecrest, California sequence. *Geophysical Research Letters*, *23*(18), 2437–2440.
Moutote, L., Marsan, D., Lengliné, O., & Duputel, Z. (2020). Low significance of foreshock activity in southern california.
Noda, H., Nakatani, M., & Hori, T. (2013). Large nucleation before large earthquakes is sometimes skipped due to cascade-up implications from a rate and state simulation of faults with hierarchical asperities. *Journal of Geophysical Research: Solid Earth*, *118*(6), 2924–2952.
Ohnaka, M. (1992). Earthquake source nucleation: a physical model for short-term precursors. *Tectonophysics*, *211*(1-4), 149–178.
Okuda, T., & Ide, S. (2018). Hierarchical rupture growth evidenced by the initial seismic waveforms. *Nature communications*, *9*(1), 1–7.
Pritchard, M. E., Allen, R. M., Becker, T. W., Behn, M. D., Brodsky, E. E., Bürgmann, R., ... others (2020). New opportunities to study earthquake precursors. *Seismological Research Letters*, *91*(20), 2444–2447.
Renard, F., Cordonnier, B., Kobchenko, M., Kandula, N., Weiss, J., & Zhu, W. (2017). Microscale characterization of rupture nucleation unravels precursors to faulting in rocks. *Earth and Planetary Science Letters*, *476*, 69–78.
Renard, F., Weiss, J., Mathiesen, J., Ben-Zion, Y., Kandula, N., & Cordonnier, B. (2018). Critical evolution of damage toward system-size failure in crystalline rock. *Journal of Geophysical Research: Solid Earth*, *123*(2), 1969–1986.
Ross, Z. E., Idini, B., Jia, Z., Stephenson, O. L., Zhong, M., Wang, X., ... Moore, A. W. (2019). Hierarchical interlocked orthogonal faulting in the 2019 Ridgecrest earthquake sequence. *Science*, *3665*(October), 346–351.
Ruiz, S., Aden-Antoniow, F., Baez, J., Otarola, C., Potin, B., del Campo, F., ... others (2017). Nucleation phase and dynamic inversion of the Mw 6.9 Valparaíso 2017 earthquake in central Chile. *Geophysical Research Letters*, *44*(20), 10–290.
Ruiz, S., Metois, M., Fuenzalida, A., Ruiz, J., Leyton, F., Grandin, R., ... Campos, J. (2014). Intense foreshocks and a slow slip event preceded the 2014 Iquique Mw 8.1 earthquake. *Science*, *345*(6201), 1165–1169. doi: 10.1126/science.1256074
Seif, S., Zechar, J. D., Mignan, A., Nandan, S., & Wiemer, S. (2019). Foreshocks and their potential deviation from general seismicity. *Bulletin of the Seismological Society of America*, *109*(1), 1–18.
Shearer, P. M., & Lin, G. (2009). Evidence for Mogi doughnut behavior in seismicity preceding small earthquakes in southern California. *Journal of Geophysical Research: Solid Earth*, *114*(B1).
Shelly, D. R. (2020). A high-resolution seismic catalog for the initial 2019 Ridgecrest earthquake sequence: foreshocks, aftershocks, and faulting complexity. *Seismological Research Letters*, *91*(4), 1971—1978.
Spudich, P., & Cranswick, E. (1984). Direct observation of rupture propagation during the 1979 Imperial Valley earthquake using a short baseline accelerometer array. *Bulletin of the Seismological Society of America*, *74*(6), 2083–2114.
Sykes, L. R., Shaw, B. E., & Scholz, C. H. (1999). Rethinking earthquake prediction. *Pure and Applied Geophysics*, *155*(2-4), 207–232. doi: 10.1007/s000240050263
Tape, C., Holtkamp, S., Silwal, V., Hawthorne, J., Kaneko, Y., Ampuero, J. P., ... West, M. E. (2018). Earthquake nucleation and fault slip complexity in the lower crust of central Alaska. *Nature Geoscience*, *11*(7), 536–541.

Tinti, E., Scuderi, M., Scognamiglio, L., Di Stefano, G., Marone, C., & Collettini, C. (2016). On the evolution of elastic properties during laboratory stick-slip experiments spanning the transition from slow slip to dynamic rupture. *Journal of Geophysical Research: Solid Earth*, *121*(12), 8569–8594.

Trugman, D. T., & Ross, Z. E. (2019). Pervasive foreshock activity across southern california. *Geophysical Research Letters*, *46*(15), 8772–8781.

Trugman, D. T., Ross, Z. E., & Johnson, P. A. (2020). Imaging stress and faulting complexity through earthquake waveform similarity. *Geophysical Research Letters*, *47*(1), e2019GL085888.

Uchide, T., & Ide, S. (2010). Scaling of earthquake rupture growth in the Parkfield area: Self-similar growth and suppression by the finite seismogenic layer. *Journal of Geophysical Research: Solid Earth*, *115*(B11).

van den Ende, M. P., & Ampuero, J.-P. (2020). On the statistical significance of foreshock sequences in southern california. *Geophysical Research Letters*, *47*(3), e2019GL086224.

Wyss, M., & Brune, J. N. (1967). The Alaska earthquake of 28 march 1964: A complex multiple rupture. *Bulletin of the Seismological Society of America*, *57*(5), 1017–1023.

Xu, S., Fukuyama, E., & Yamashita, F. (2019). Robust estimation of rupture properties at propagating front of laboratory earthquakes. *Journal of Geophysical Research: Solid Earth*, *124*(1), 766–787. doi: 10.1029/2018JB016797

Yamashita, T. (2000). Generation of microcracks by dynamic shear rupture and its effects on rupture growth and elastic wave radiation. *Geophysical Journal International*, *143*(2), 395–406.

Yao, D., Huang, Y., Peng, Z., & Castro, R. R. (2020). Detailed investigation of the foreshock sequence of the 2010 Mw 7.2 El Mayor-Cucapah earthquake. *Journal of Geophysical Research: Solid Earth*, *125*(6), e2019JB019076.

Yoon, C. E., Yoshimitsu, N., Ellsworth, W. L., & Beroza, G. C. (2019). Foreshocks and mainshock nucleation of the 1999 Mw 7.1 Hector Mine, california, earthquake. *Journal of Geophysical Research: Solid Earth*, *124*(2), 1569–1582.

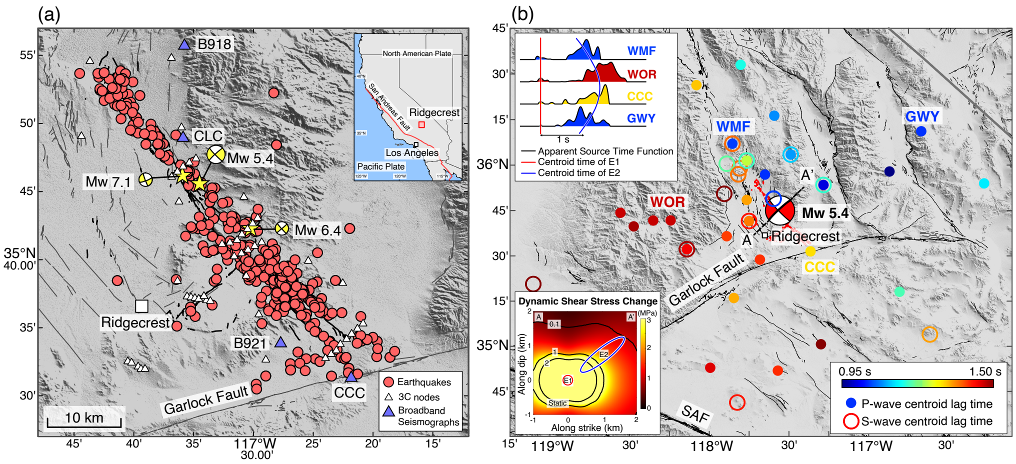

Figure 1. (a) Earthquakes with immediate-foreshocks. White triangles are the nodal stations (Catchings et al., 2020) and blue triangles are four broadband seismographs (Caltech.Dataset., 2013). Fault traces are identified from geodetic observations (Jin & Fialko, 2020). The inset shows a regional map of California. (b) The centroid lag time distribution of the two subevents of the M_w 5.4 earthquake. The earthquake rupture propagated towards the northeast direction, perpendicular to the M_w 7.1 earthquake fault strike. The top-left inset shows four example apparent source time functions of the M_w 5.4 earthquake at different azimuths. The bottom left inset shows the stress perturbations at the subevent E2 from the subevent E1 (Figure S2). The color and contour show the peak dynamic- and static-stress perturbations respectively.

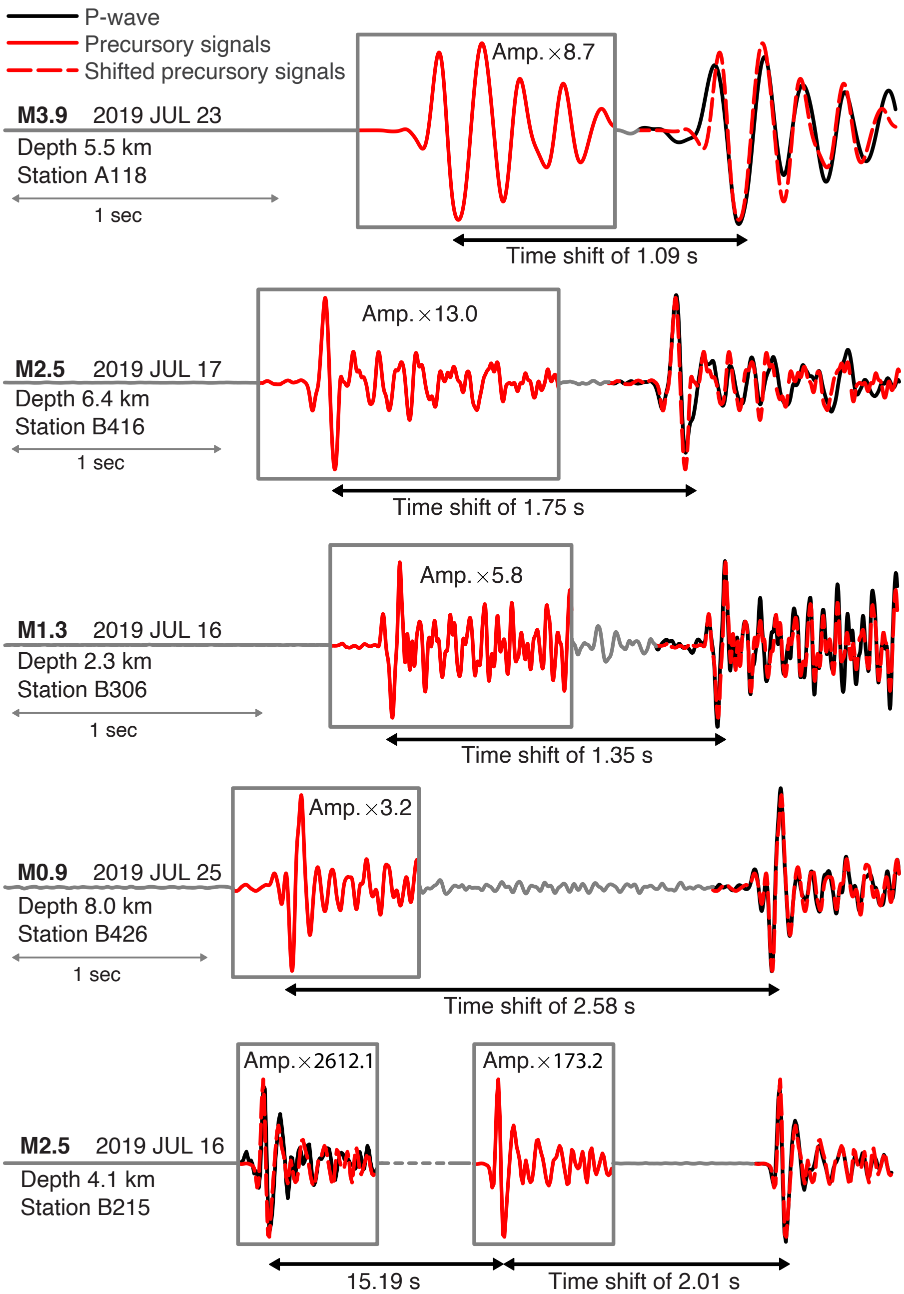

Figure 2. Example earthquake P-waves and their precursory signals from the immediate-foreshocks recorded by the nodal stations. The precursory signals are highlighted by the gray boxes and amplified for visual comparisons. The amplification factors are listed in the boxes. The records are the vertical-components of example nodal array stations and the waveforms are band-pass filtered at 1 to 20 Hz with a casual 2nd-order Butterworth filter. The amplitude ratio and preceding time distributions for each event are shown in Figures S4 and S5.

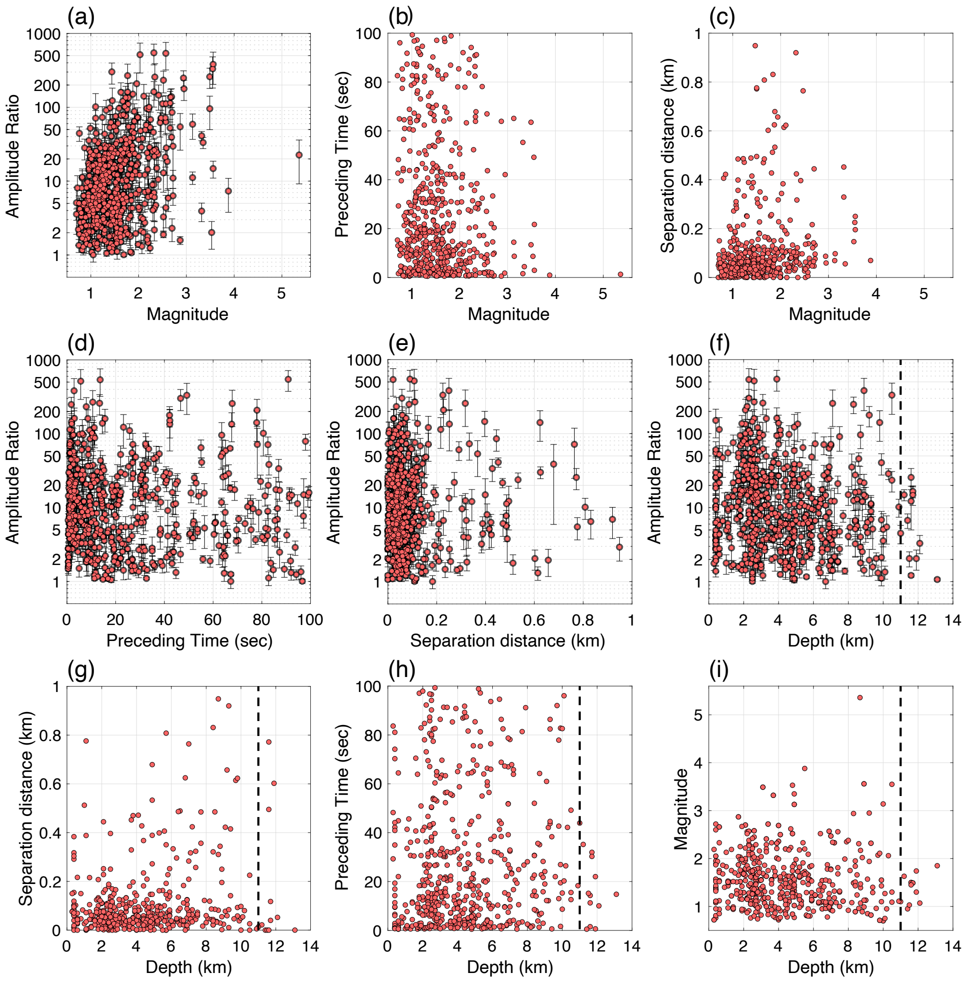

Figure 3. Scatter plots of the measured amplitude ratio, preceding time, magnitude, hypocentral separation, and depth of the earthquakes and their immediate-foreshocks. The amplitude ratio error bar shows one standard deviation of the measurements for a given earthquake. The dashed line is the 95 percentile seismicity depth, 11.0 km (Text S3).

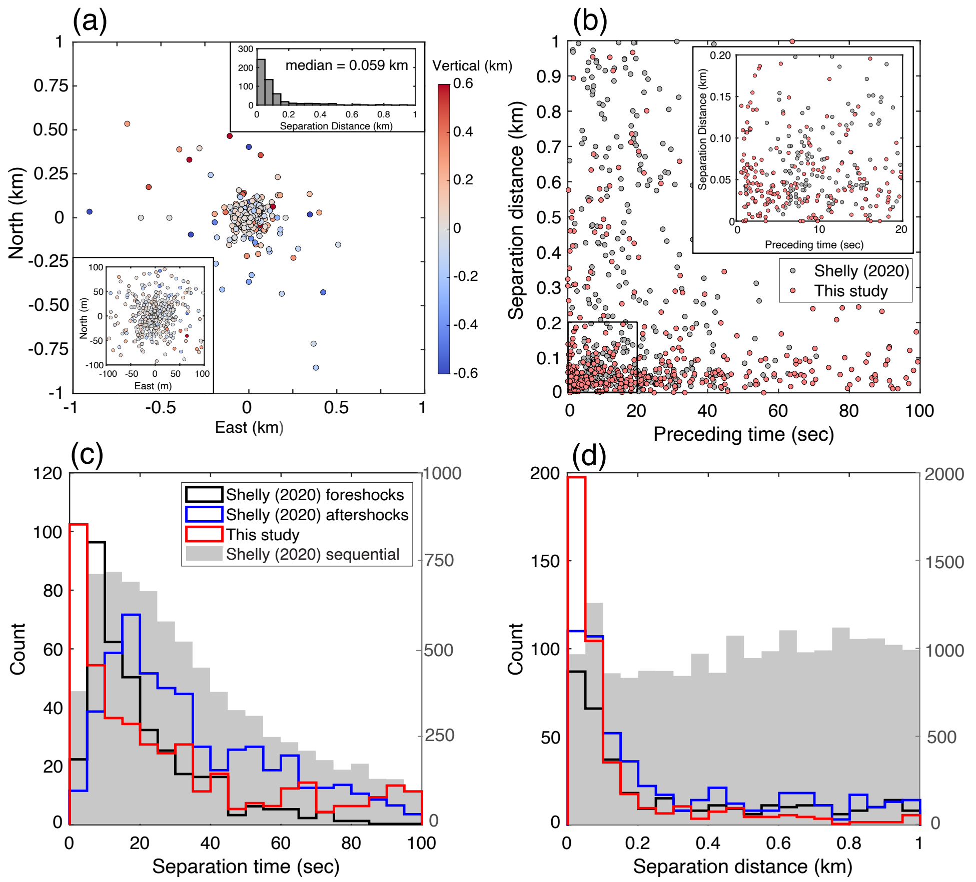

Figure 4. (a) Horizontal and vertical the separations of the immediate-foreshocks to the mainshocks. The bottom left insert shows the zoomed-in view of the hypocentral separations. The top right insert shows the histogram of separation distances with a median of 0.059 km. (b) Preceding time and separation distance of the immediate-foreshocks detected in this study and the selected foreshocks in a local high-resolution catalog (Shelly, 2020). The foreshocks are selected with preceding time less than 100 seconds and spatial separation less than 1 km of the mainshocks. (c) and (d) Distributions of separation time and distance to the mainshocks of the immediate-foreshocks detected in this study and foreshocks aftershocks in Shelly's catalog. The foreshocks and aftershocks sequences are defined as two or more events occurring spatiotemporally within 100 s and 1 km, and the foreshock or aftershock magnitudes are smaller than those of the mainshocks. The gray histograms show the separation distance and time for sequential earthquake pairs in Shelly's catalog within 1 km hypocentral distance of the 527 events with detected immediate-foreshocks.

Supporting Information for "Immediate-foreshocks indicating a common cascading earthquake rupture development"

Haoran Meng[1] **and Wenyuan Fan**[1]

[1]Scripps Institution of Oceanography, UC San Diego, La Jolla, CA 92093-0225, USA

Contents of this file

Text S1. Second moments analysis

We perform empirical Green's function (eGf) analysis to obtain the apparent source time functions (ASTFs) for the M_w 5.4 earthquake. We obtain the ASTFs individually at each station by deconvolving seismograms of the M_w 5.4 event with those of a nearby M 3.7 earthquake to remove the path and site effects for both P- and S-waves (Figures S2). We use stations from the regional broadband networks and the strong motion networks to investigate the earthquake. The seismic records are band-pass filtered at 0.5 to 20.0 Hz with a causal 2nd-order Butterworth filter. The ASTFs show clearly separated episodes indicating two major subevents E1 and E2. The seismic moments of E1 and E2 are estimated by computing an average moment ratio between the two episodes and requiring the total moment equal to that of a M_w 5.4 earthquake. For each ASTF, a moment ratio is obtained from dividing the subevent moments, which are integrations of the episodes respectively (Figure S2a). The moment ratio of E1 to E2 is about 5%, equivalent to a M_w 4.5 earthquake for E1. We further estimate the centroid location separation distance by curve fitting the centroid lag time at different directions (Figures 1b and S2). The centroid location of E2 is 1.1 km northeast of E1, showing that the earthquake ruptured a fault plane that is orthogonal to the main fault strike of the M_w7.1 mianshock (Shelly, 2020).

With the ASTFs and a local 1D velocity model, we solve the rupture length and width of the subevent E2 by estimating its second seismic moments. The 1D velocity model is obtained from averaging the community velocity model of Southern California (Lee et al., 2014). We closely follow a method that is used to study the second moments of other Southern California earthquakes (Meng et al., 2020; McGuire, 2004, 2017), and only briefly explain the physical meanings of the second moments here. Centroid location and centroid time are the first moments of an earthquake, and the second seismic moments characterize the variances of the first moments, which effectively represent the earthquake length, width, duration and rupture directivity (Backus & Mulcahy, 1976a, 1976b; McGuire, 2004). Knowing the local velocity structure, the second seismic moments $\underline{\underline{\widehat{\mu}}}^{(2,0)}$, $\widehat{\mu}^{(0,2)}$, and $\underline{\widehat{\mu}}^{(1,1)}$ can be obtained by solving:

$$\widehat{\mu}^{(0,2)}(\underline{s}) = \widehat{\mu}^{(0,2)} - 2\underline{s} \cdot \widehat{\mu}^{(1,1)} + \underline{s} \cdot \underline{\underline{\widehat{\mu}}}^{(2,0)}\underline{s} \tag{1}$$

where $\widehat{\mu}^{(0,2)}(\underline{s})$ is the apparent duration obtained from the ASTF and $\underline{s}$ is the slowness of either P- or S-waves in the source region for a given source-receiver pair (McGuire, 2004). The second moments can estimate an earthquake characteristic duration ($\tau_c = 2\sqrt{\widehat{\mu}^{(0,2)}}$) and earthquake characteristic rupture extents ($x_c(\underline{\widehat{n}}) = 2\sqrt{\underline{\widehat{n}}^T \underline{\underline{\widehat{\mu}}}^{(2,0)} \underline{\widehat{n}}}$), where $\underline{\widehat{n}}$ is a unit eigenvector of $\underline{\underline{\widehat{\mu}}}^{(2,0)}$ and x_c represents the associated rupture dimension, e.g., the rupture length L_c or the rupture width W_c (McGuire, 2004).

Following a case study of the 1999 Izmit, Turkey M_w 7.6 earthquake and its foreshocks (Ellsworth, 2019), we estimate the stress perturbations from E1 to E2. We approximate the subevent E1 as a M_w 4.5 earthquake (point source) with the same focal mechanism of the M_w 5.4 earthquake, and assume the E1 source time function as a parabola function lasting 0.3 s. We then synthesize a 3D displacement field of E1 in a whole-space homogeneous medium with $V_p = 6.169$ km/s, $V_s = 3.523$ km/s, and $\rho = 2,600$ kg/m^3 (Aki & Richards, 2002) (Figure S3). The 3D model space is set as 4,000 m along strike by 4,000 m along dip by 40 m perpendicular to the fault surface with a grid spacing of 20 m and the subevent E1 is set in the center of the model space. We calculate the three-component displacements at each grid for 2 seconds with a sampling rate of 500 Hz to account for both the transient- and permanent-displacement. The strain-tensor perturbations on the fault plane are computed as numerical spatial derivatives of the displacement field. We then use the Hooke's law to obtain the stress perturbations. The fault-plane normal stress perturbations are zero and the static and peak dynamic shear stress perturbations exceed 0.1 MPa in the vicinity of the subevent E2 (Figures 2 and S3).

Text S2. Detection of immediate-foreshocks

We detect immediate-foreshocks by using the vertical component records and autocorrelating the P-waves with their 100 s preceding waveforms. The seismic records are band-pass filtered at 1 to 20 Hz with a causal 2nd-order Butterworth filter. With a regional catalog (SCEDC; Hutton et al., 2010), the P-wave arrival times are first calculated using a 1D velocity model, which is obtained from averaging the community velocity model of Southern California (Lee et al., 2014). The P-wave onset times are then further refined with manual corrections. The autocorrelation is performed independently for all stations within epicentral distance of 30 km, including both the regional network stations, the rapid deployment broadband stations, and the nodal array stations. For a given station, we test a set of P-wave time windows from 0.5 s to 1.0 s with an incremental step of 0.1 s, and the preferred time window of the event-station pair maximizes the autocorrelation coefficient (AC).

For a given event, we select candidate stations with maximum AC greater than 0.7, and record the autocorrelation differential time (signal preceding time) and the amplitude ratio in addition to the autocorrelation coefficient. For $M \leq 3.5$ earthquakes, an immediate-foreshock is detected when (1), the average AC exceeds 0.8 for more than 10 stations; (2), these stations are from an azimuthal range greater than 180°; (3), the preceding time distribution has a standard deviation less than 0.01 s. For $3.5 \leq M \leq 5.0$ earthquakes (there are only 3 events), we impose a similar set of criteria, including (1), the average AC exceeds 0.7 for more than 10 stations; (2), these stations are from an azimuthal range greater than 180°; (3), the preceding time distribution has a standard deviation that is less than 0.05 s. P-waves are more complex for larger magnitude earthquakes, and this modification allows us to effectively search immediate-foreshocks for all earthquakes with $0.5 \leq M \leq 5.4$. In total, we find 527 earthquakes with clear immediate-foreshocks and do not observe a magnitude dependence of the measured amplitude ratio or the preceding time.

The three-component nodal stations are short-period seismographs with a natural frequency of 5 Hz. Because of the natural frequency, the instruments may fail to record the low frequency (≤5 Hz) ground motion faithfully. Additionally, the band-pass filter (1-20 Hz) used in the analysis may introduce possible biases. To evaluate these potential biases, we compare the records of four earthquakes from M 2.5 to M 4.0 at a pair of collocated seismographs, including a broadband station CA03 and a nodal station U01 (Figure S11). We first remove the instrumental responses and then band-pass filter the records at 0.2 to 45 Hz with a causal 2nd-order Butterworth filter. The two sensors recorded almost identical ground motions and the results show that the nodal stations can record the investigated earthquakes with high fidelity. Given the noise level and the site conditions of the nodal stations, the 1-20 Hz band-pass filter can effectively suppress the high-frequency noise, and it does not impact small earthquake amplitudes very much. Our results show that the nodal array stations recorded high-quality data, and they can be used to investigate a range of earthquake rupture features.

Text S3. Estimating the creeping transition depth

Following the standard approach (Magistrale, 2002; Rolandone et al., 2004), we estimate the deep creeping transition depth as the 95 percent earthquake depth threshold. In this study, the seismogenic zone depth extent is estimated as 11.0 km from a regional catalog of the 2019 Ridgecrest sequence (SCEDC; Hutton et al., 2010).

Text S4. Relative location of the immediate-foreshocks

We determine the relative locations between the immediate-foreshocks and the mainshocks using the differential times measured at multiple seismic stations. We first compute the slowness of the P-wave in the source region with a 1D velocity model, which is obtained from averaging the community velocity model of Southern California (Lee et al., 2014). The preceding time t_j of the precursory signal from an immediate-foreshock i at station j and the location of the immediate-foreshock are linked as

$$t_j = \Delta \underline{r}_i \cdot \underline{s}_{ij} + t_{0j} \tag{2}$$

where $\Delta \underline{r}_i$ is the relative location between the ith pair of the immediate-foreshock and the mainshock, $\underline{s}_{ij}$ is the slowness vector of P-wave in the source region of the seismic ray-path connecting the mainshock hypocenter and the seismograph j, and t_{0j} is the preceding time of the immediate-foreshock. With multiple measurements of t_j, the relative location and preceding origin time can be determined using the equation above. With the relative locations, we found most of these foreshocks are located within 0.2 km of their mainshocks with a median separation of 59 m (Figure 4a).

We further evaluate the uncertainties of the relative locations by performing jackknife-resampling of the stations (Efron & Tibshirani, 1994). For each realization, we remove one measurement t_j and perform inversion with the remaining measurements. For a given separation distance (e.g., the vertical separation distance) or origin time m, $\hat{m}_j$ is the jth jackknife realization of m and $\hat{m}$ is the mean of $\hat{m}_j$:

$$\hat{m} = \frac{1}{N} \sum_{i=1}^{N} \hat{m}_j \tag{3}$$

where N is the total number of measurements. The jackknife estimate of the standard deviation ($\hat{m}_\sigma$) of m is computed as

$$\hat{m}_\sigma = \sqrt{\frac{N-1}{N} \sum_{i=1}^{N} (\hat{m}_j - \hat{m})^2} \tag{4}$$

We estimate the standard deviations (uncertainties) at three directions independently for the hypocentral separations of the 527 immediate-foreshock and the mainshock pairs (Figure S7). About 85% of the separation distance between the immediate-foreshocks and mainshocks has a standard deviation less than 0.1 km with a median value of 15 m horizontally (Figure S7f). Vertically, 78% of the separation distance has a standard deviation less than 0.1 km with a median value of 31 m (Figure S7f).

Text S5. Foreshock-mainshock and mainshock-aftershock sequences in a local high resolution catalog

We use a catalog that is obtained with a template matching technique (Shelly, 2020) to investigate the foreshock-mainshock and mainshock-aftershock sequences of the Ridgecrest earthquakes. The high resolution catalog reports 34,091 $-0.3 \leq M \leq 7.1$ earthquakes occurring from 4 July 2019 to 16 July 2019 in the Ridgecrest region (Shelly, 2020). For a given earthquake, we search for events preceding the target earthquake within 100 s and within 1 km hypocentral distance. If these events have magnitudes smaller than the target earthquake, they are considered as foreshocks of the target earthquake. In total, there are 524 candidate foreshock-mainshock sequences with one or more foreshocks. Out of the 524 candidates, 363 foreshock-mainshock sequences are further confirmed by visual inspections of the nodal array waveforms, and we focus on analyzing these cases. Out of the 363 earthquakes, 16 events have more than one foreshocks and the remaining earthquakes only have a single foreshock. There are no clear migration patterns of the foreshock-mainshock sequences. The preceding time, magnitude, hypocentral separation and depth of these foreshocks show similar characteristics to the 527 immediate-foreshocks reported in this study (Figures S8 and 3). We also search for earthquakes with smaller magnitudes within 100 s after a target earthquake and within 1 km hypocentral distance. These events are considered aftershocks. In total, we find 519 mainshock-aftershock sequences in Shelly (2020).

Text S6. Inverse Omori's law

We evaluate the frequencies of the 527 immediate-foreshocks reported in this study and the 363 foreshocks in Shelly (2020). The seismicity rate is evaluated by binning the event occurrence in 5 seconds non-overlapping bins up to 100 seconds preceding the main events (Figure S9). Both the immediate-foreshocks and the foreshocks occur more frequently as the mainshock approaches, following an exponential increase trend. Assuming such increases follow an inverse Omori's law, $k/(-t)^p$, where k is a productivity constant and p is the growing rate, we perform a grid search on these two parameters to fit the two parameters for both catalogs respectively. We found a growing rate of $p = 0.57$ for the 527 immediate-foreshocks and a rate of $p = 0.89$ for the 363 foreshocks in the Shelly (2020) catalog. The the different p-values may indicate a possible difference in triggering efficiency at different scales (Figure 4). However, the physical meaning of the p parameter is unclear and we do not discuss the details in this paper (Shcherbakov et al., 2004).

Text S7. Data and materials

The earthquake catalogs were accessed from Southern California Earthquake Data Center (SCEDC; Hutton et al., 2010) and Shelly (2020). The seismic data were provided by Data Management Center (DMC) of the Incorporated Research Institutions for Seismology (IRIS) and the SCEDC (Caltech.Dataset., 2013). The facilities of IRIS Data Services, and specifically the IRIS Data Management Center, were used for access to waveforms, related metadata, and/or derived products used in this study. IRIS Data Services are funded through the Seismological Facilities for the Advancement of Geoscience and EarthScope (SAGE) Proposal of the National Science Foundation (NSF) under Cooperative Agreement EAR-1261681. The nodal array data is openly available through IRIS DMC and was acquired by the U.S. Geological Survey (USGS) (Catchings et al., 2020) and the Southern California Earthquake Center (SCEC) and SCEC member institutions. The experiments were led by Rufus D. Catchings and Mark R. Goldman. The rapid seismic deployment of nodes for the 2019 Ridgecrest earthquake sequence was partially supported by the U.S. Geological Survey (USGS), the Southern California Earthquake Center, and the National Science Foundation (Grant Number EAR-1945781).

Table 1. 527 earthquakes with immediate-foreshocks. The event ID and locations are from the SCEDC catalog (Hutton et al., 2010).

References

Aki, K. (1965). Maximum likelihood estimate of b in the formula log n= a-bm and its confidence limits. *Bull. Earthq. Res. Inst., Tokyo Univ.*, *43*, 237–239.

Aki, K., & Richards, P. G. (2002). *Quantitative seismology.*

Backus, G., & Mulcahy, M. (1976a). Moment tensors and other phenomenological descriptions of seismic sources–I. continuous displacements. *Geophysical Journal International*, *46*(2), 341–361. doi: 10.1111/j.1365-246x.1976.tb04162.x

Backus, G., & Mulcahy, M. (1976b). Moment tensors and other phenomenological descriptions of seismic sources–II. discontinuous displacements. *Geophysical Journal International*, *47*(2), 301–329. doi: 10.1111/j.1365-246x.1976.tb01275.x

Caltech.Dataset. (2013). Southern California Earthquake Data Center. doi: 10.7909/C3WD3xH1

Catchings, R. D., Goldman, M., Steidl, J., Chan, J., Allam, A., Criley, C., ... Ben-Zion, Y. (2020). Nodal seismograph recordings of the 2019 Ridgecrest earthquake sequence. *Seismological Research Letters*, *91*(6), 3622—3633.

Efron, B., & Tibshirani, R. J. (1994). *An introduction to the bootstrap.* CRC press.

Ellsworth, W. L. (2019). From foreshocks to mainshocks: mechanisms and implications for earthquake nucleation and rupture propagation. *Mechanics of Earthquake Faulting*, *202*, 95.

Hutton, K., Woessner, J., & Hauksson, E. (2010). Earthquake monitoring in southern california for seventy-seven years (1932–2008). *Bulletin of the Seismological Society of America*, *100*(2), 423–446.

Lee, E.-J., Chen, P., Jordan, T. H., Maechling, P. B., Denolle, M. A., & Beroza, G. C. (2014). Full-3-D tomography for crustal structure in southern California based on the scattering-integral and the adjoint-wavefield methods. *Journal of Geophysical Research: Solid Earth*, *119*(8), 6421–6451.

Magistrale, H. (2002). Relative contributions of crustal temperature and composition to controlling the depth of earthquakes in southern California. *Geophysical research letters*, *29*(10), 87–1.

McGuire, J. J. (2004). Estimating finite source properties of small earthquake ruptures. *Bulletin of the Seismological Society of America*, *94*(2), 377–393. doi: 10.1785/0120030091

McGuire, J. J. (2017). A MATLAB toolbox for estimating the second moments of earthquake ruptures. *Seismological Research Letters*, *88*(2A), 371–378. doi: 10.1785/0220160170

Meng, H., McGuire, J. J., & Ben-Zion, Y. (2020). Semiautomated estimates of directivity and related source properties of small to moderate southern California earthquakes using second seismic moments. *Journal of Geophysical Research: Solid Earth*, *125*(4), e2019JB018566.

Rolandone, F., Bürgmann, R., & Nadeau, R. (2004). The evolution of the seismic-aseismic transition during the earthquake cycle: constraints from the time-dependent depth distribution of aftershocks. *Geophysical Research Letters*, *31*(23).

Shcherbakov, R., Turcotte, D. L., & Rundle, J. B. (2004). A generalized omori's law for earthquake aftershock decay. *Geophysical research letters*, *31*(11).

Shelly, D. R. (2020). A high-resolution seismic catalog for the initial 2019 Ridgecrest earthquake sequence: foreshocks, aftershocks, and faulting complexity. *Seismological Research Letters*, *91*(4), 1971—1978.

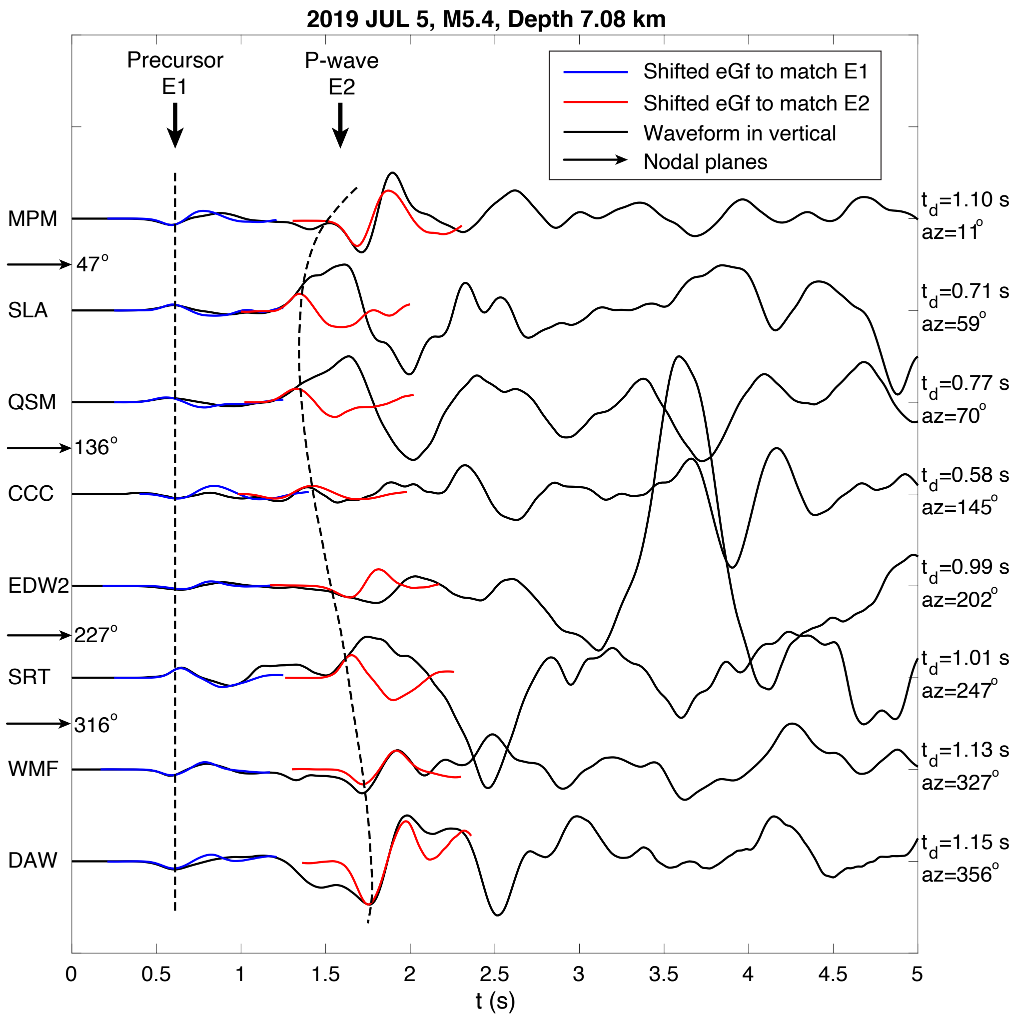

Figure S1. Precursory signals and P-waves of the M_w 5.4 earthquake at eight example broadband stations. The waveforms are from the vertical-component records and are band-pass filtered at 0.2 to 20 Hz with a causal 2nd-order Butterworth filter. The traces are aligned with their station azimuths. The station names and azimuthal directions are listed by the traces. az stands for the azimuth and t_d is the preceding time. The blue and red curves are scaled P-waves of a nearby M 3.7 eGf. Arrows show the nodal plane directions of the M_w 5.4 earthquake. The black dash-curves show the arrival times of the two subevents E1 and E2 with the first event aligned at 0.6 seconds. The differential arrival times suggest a northeast rupture propagation.

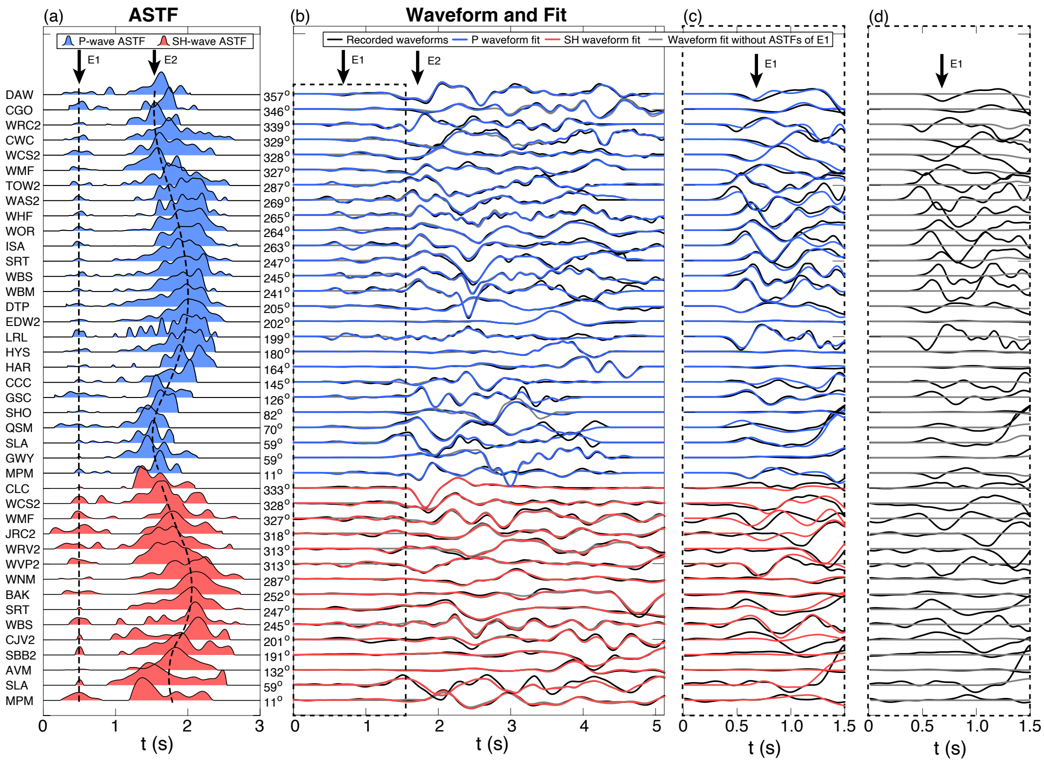

Figure S2. The apparent source time functions (ASTFs) and the waveform fit of the M_w 5.4 earthquake. (a) The ASTFs of P-waves (blue) and SH-waves (red). The black dash-curves show the centroid lag times at different stations (see Figure 2). The early small pulses are the ASTFs of subevent E1 and the later strong pulses are the ASTFs of subevent E2. (b) Waveforms of the observed and synthesized P- and SH-waves. The black traces are observations recorded by regional broadband and strong motion seismographs, the blue traces are synthetic P-waves, and the red traces are synthetic SH-waves. The gray traces are the synthetic waveforms by suppressing the ASTFs of E1. (c) and (d) The zoomed-in view of the waveforms and synthetics of E1. The observations cannot be recovered by the synthetics without the ASTFs of E1.

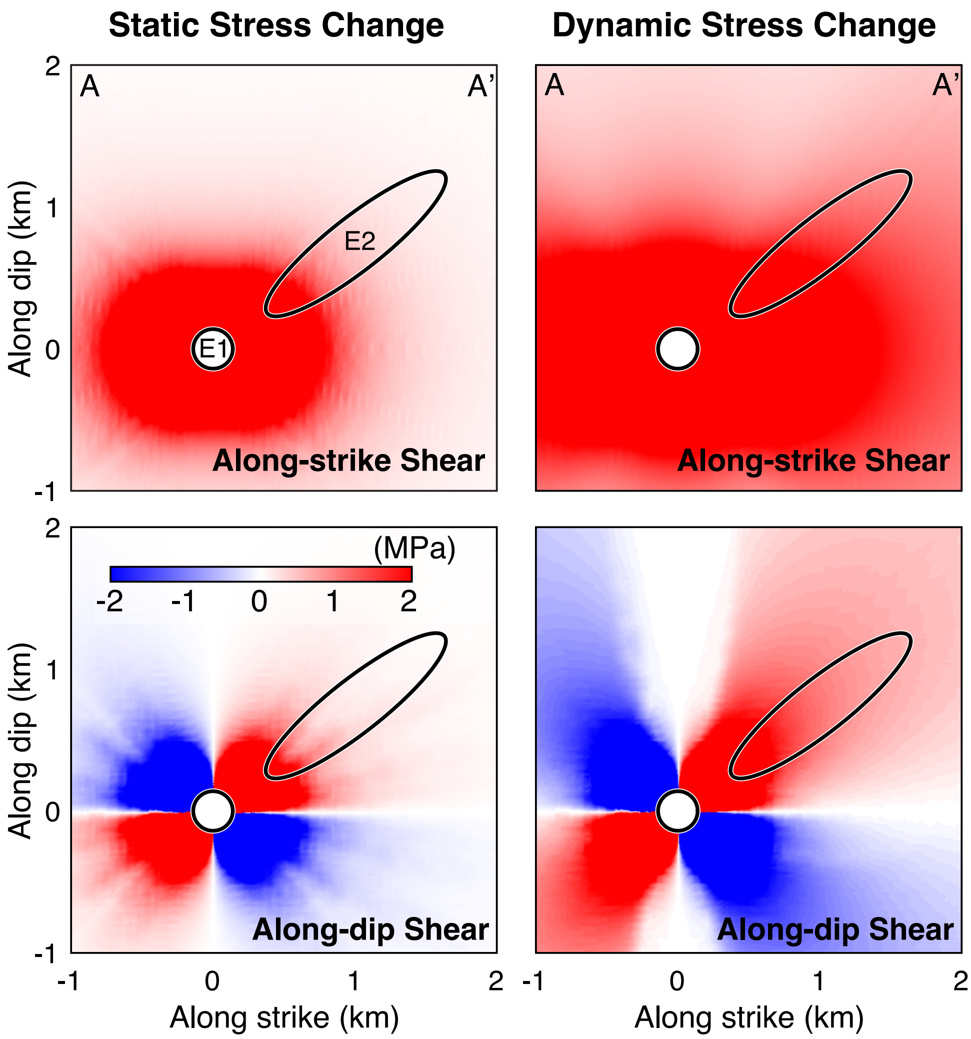

Figure S3. Static and peak dynamic shear stress perturbations from E1 to E2 of the M_w 5.4 earthquake on a 42°-strike fault plane. The static and dynamic normal stress changes are zero.

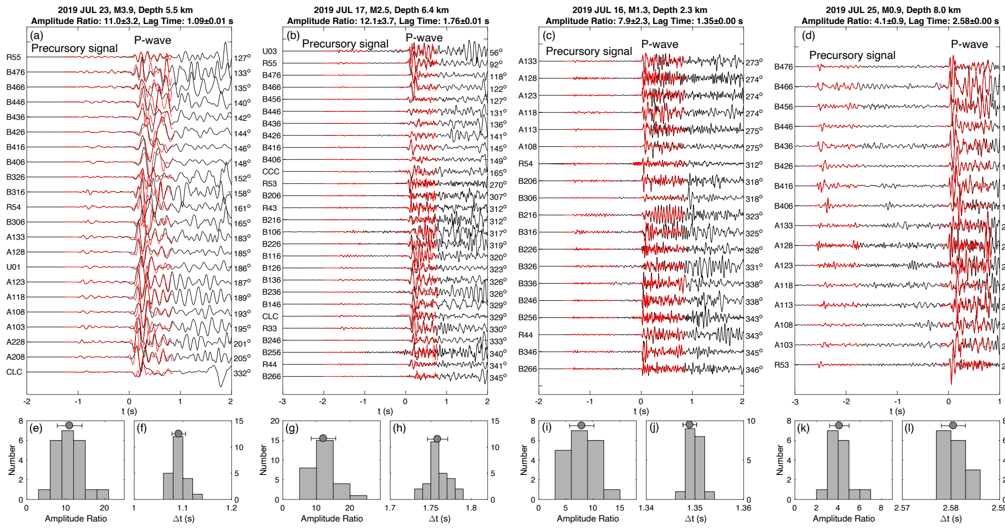

Figure S4. (a) Precursory signals and P-waves of a M 3.9 earthquake (Figure 2). The earthquake event ID is 38627095 (35.74567°/−117.55800°/5.5 km). (b) Precursory signals and P-waves of a M 2.5 earthquake. The earthquake event ID is 38592095 (35.64167°/ − 117.47150°/6.4 km). (c) Precursory signals and P-waves of a M 1.3 earthquake. The earthquake event ID is 38580791 (35.61883°/ − 117.46617°/2.3 km). (d) Precursory signals and P-waves of a M 0.9 earthquake. The earthquake event ID is 38641623 (35.60983°/ − 117.45650°/8.0 km) (SCEDC; Hutton et al., 2010). The waveforms are recorded by the nodal array stations and they are band-pass filtered at 1 to 20 Hz with a causal 2nd-order Butterworth filter. The station names and station azimuths (az) are listed by the traces. (e) to (l) The corresponding amplitude ratio and preceding time (Δt) distributions of (a) to (d). The gray circle and error-bar show the mean and one standard deviation of the amplitude ratio or the preceding time.

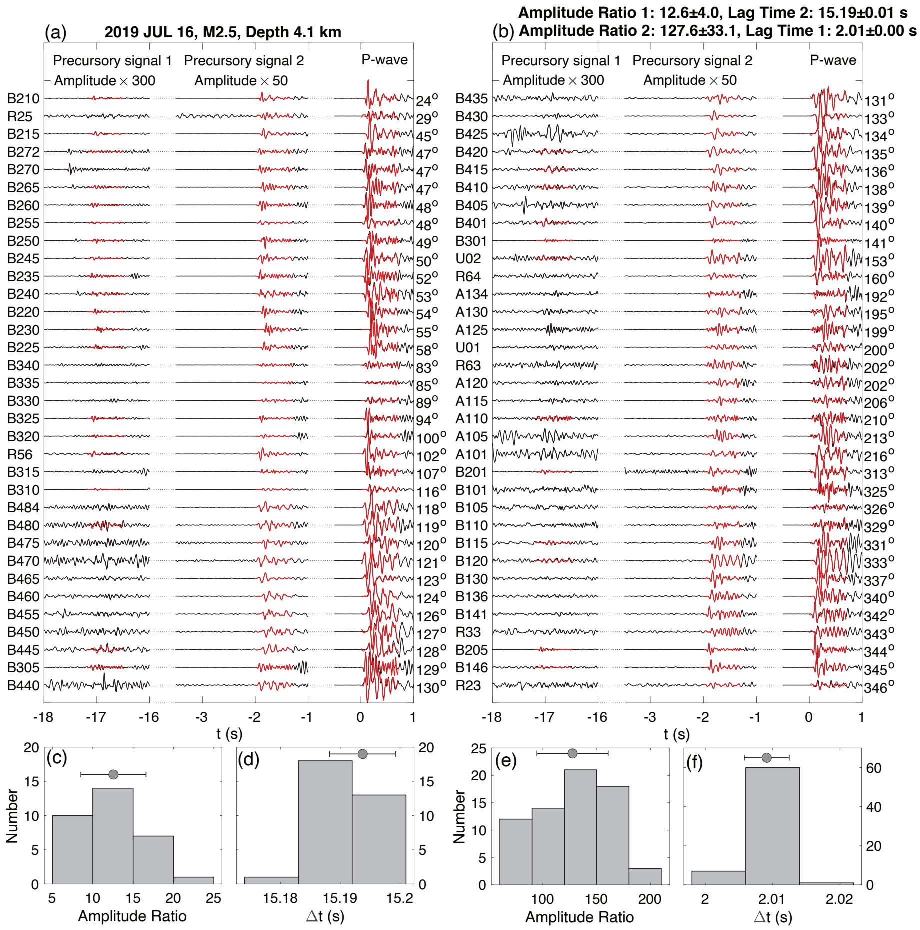

Figure S5. (a) and (b) Successive precursory signals and P-waves of a M 2.5 earthquake. The earthquake event ID is 38582951 (35.68017°/ − 117.54300°/4.1 km) (SCEDC; Hutton et al., 2010). The waveforms are recorded by the nodal array stations and are band-pass filtered at 1 to 20 Hz. (c) and (d) Corresponding amplitude ratio and preceding time distributions of precursory signals 1 and 2. (e) and (f) Corresponding amplitude ratio and preceding time distributions of precursory signal 2 and P-wave. The gray circles and error-bars show the mean and one standard deviation of the amplitude ratio or the preceding time.

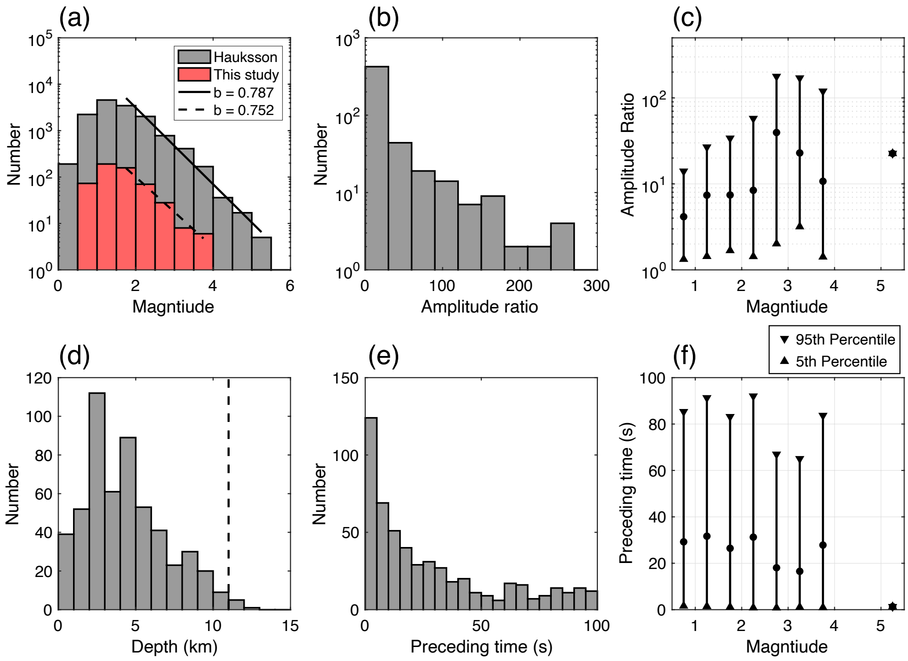

Figure S6. (a) The magnitude-frequency distribution of the 13,895 analyzed earthquakes and 527 events with observed immediate-foreshocks. (b), (d) and (e) The distributions of amplitude ratio, depth, and preceding times of the 527 events with observed immediate-foreshocks. The magnitude-frequency distribution of the earthquakes with immediate-foreshocks is statistically similar to that of the investigated earthquakes. The solid and dashed black lines in (a) show b-values of all analyzed earthquakes and events with immediate-foreshocks 0.787 and 0.752 respectively (Aki, 1965). We use earthquakes with magnitudes from 1.5 to 5.5 to estimate the b-values. (c) and (f) The range of the amplitude ratio and the preceding time of earthquakes with different magnitudes. Earthquakes are binned with a 0.5 magnitude interval from 0.5 to 5.5. The bars show 5 and 95 percentiles of the measurable. The dashed line is the 95 percentile seismicity depth, 11.0 km (Text S3).

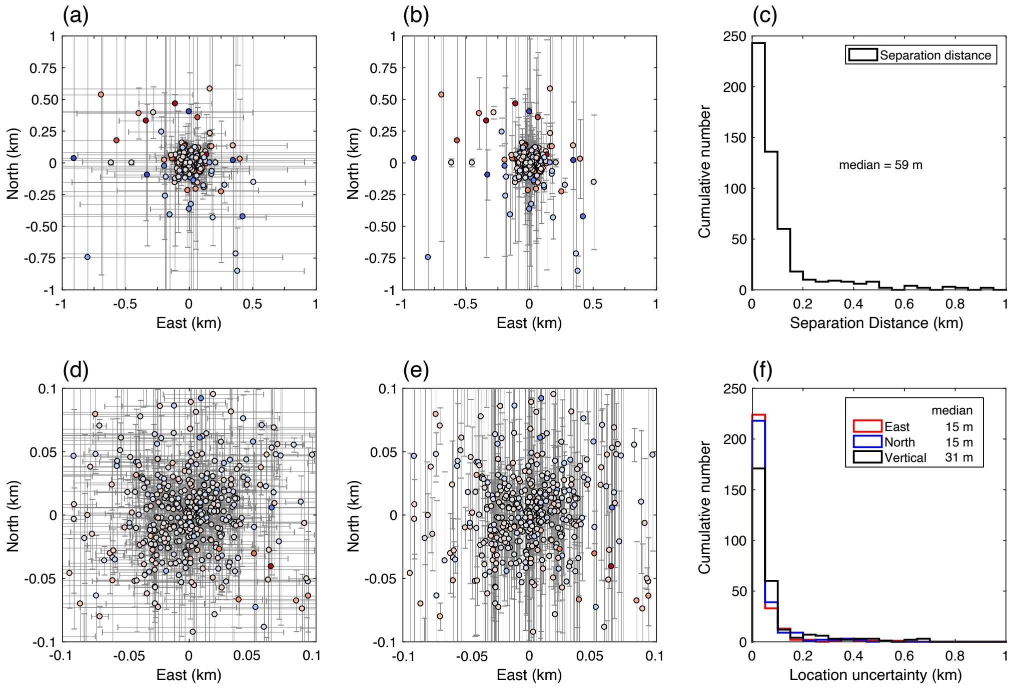

Figure S7. (a) Horizontal and vertical the separations of the immediate-foreshocks to the mainshocks. The error bars show the location uncertainties in the east and north component estimated using jackknife-resampling method (Text S4). (b) Similar to (a), but with the error bars showing the location uncertainties in the vertical component. (c) A histogram of the hypocentral separations between the immediate-foreshocks and the mainshocks. (d) and (e) The zoomed-in views of (a) and (b). (f) The histograms of location uncertainties in east, north, and vertical component.

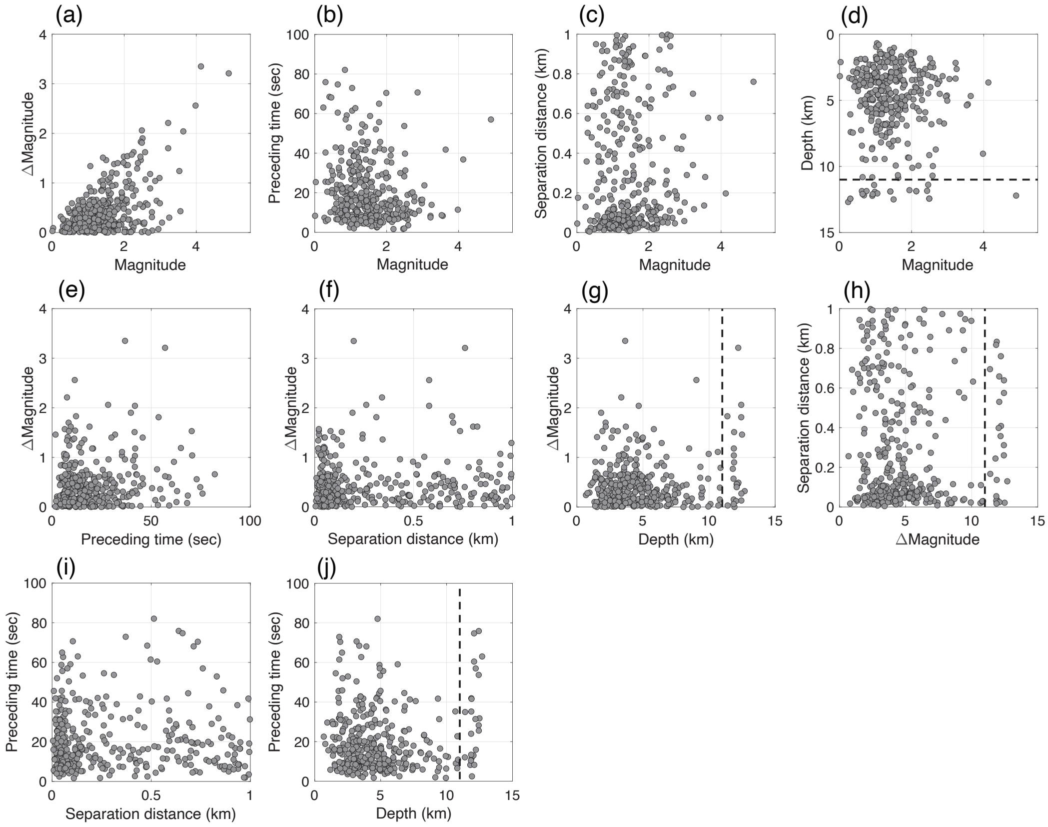

Figure S8. Scatter plots of the differential magnitude, preceding time, magnitude, hypocentral separation, and depth of the 363 foreshock-mainshock sequences in a local high-resolution catalog (Shelly, 2020). The dashed line is the 95 percentile seismicity depth, 11.0 km (Text S3).

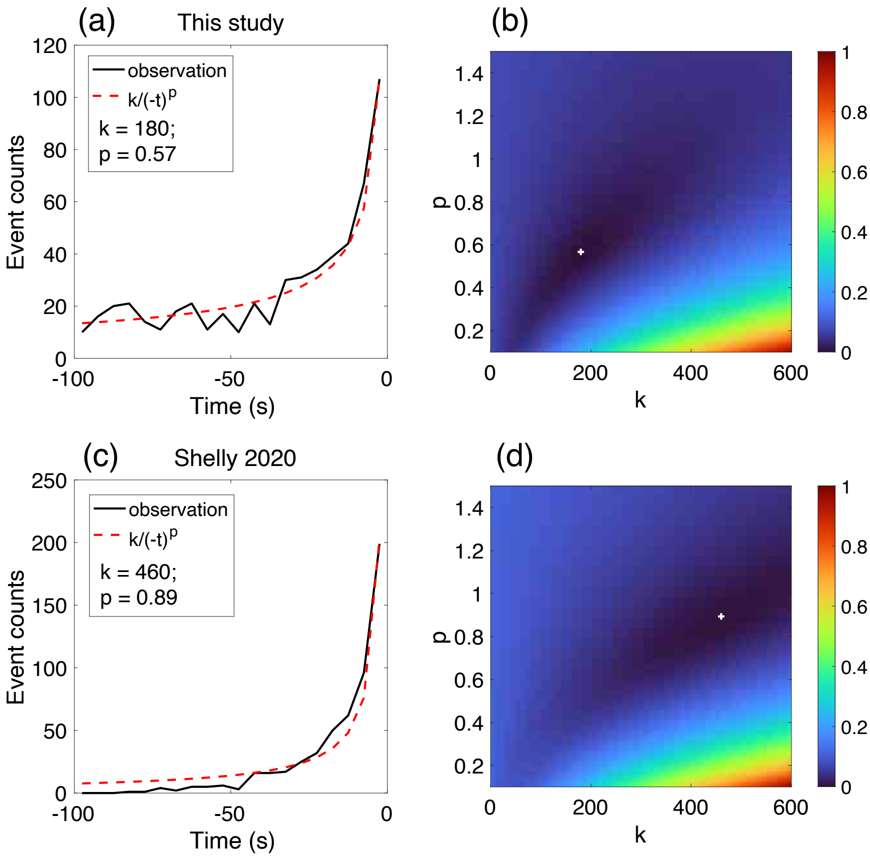

Figure S9. Event occurrence and inverse Omori law fits. (a) Differential time distribution of the immediate-foreshocks detected in this study and the inverse Omori law fit. (b) Normalized residuals by performing grid search on k and p, $p = 0.57$ for the best fit. (c) Differential time distribution of foreshocks in Shelly (2020) and the inverse Omori law fit. The foreshocks are selected with preceding time less than 100 seconds and spatial separation less than 1 km of the mainshocks. (c) Normalized residuals by performing grid search on k and p, $p = 0.89$ for the best fit.

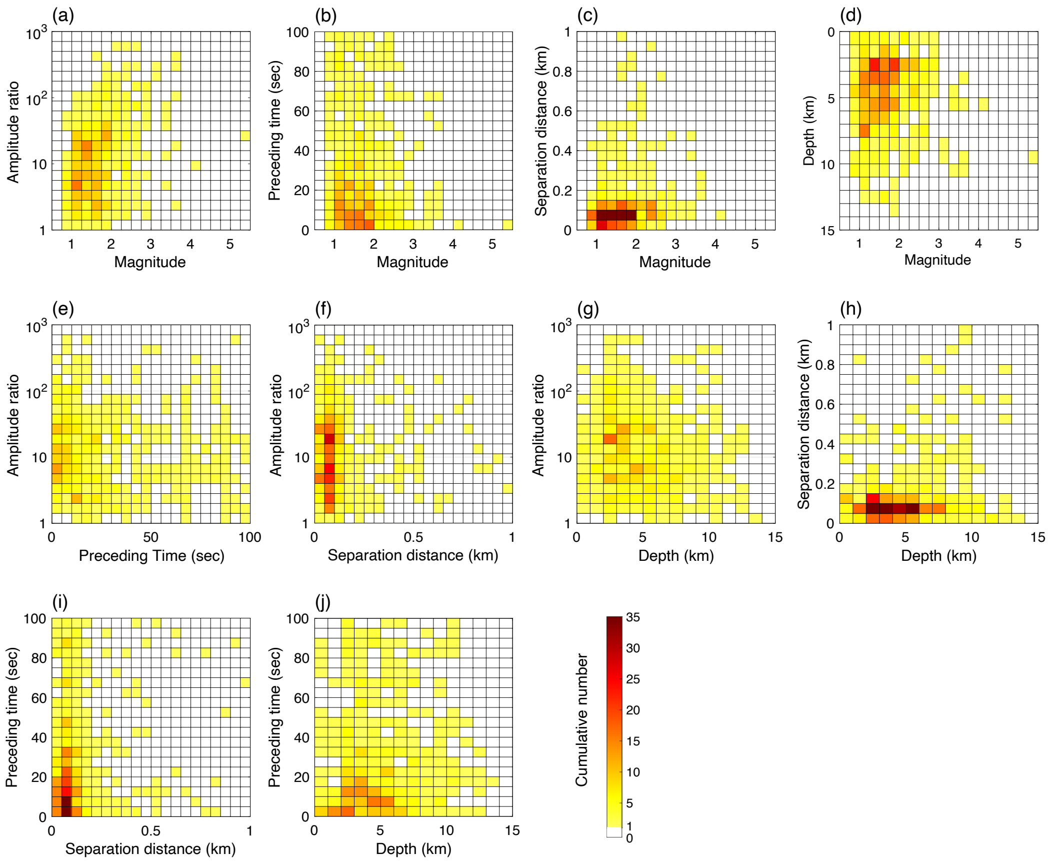

Figure S10. Earthquake density plots of the measured amplitude ratio, preceding time, magnitude, hypocentral separation, and depth of the 527 earthquakes with their observed immediate-foreshocks.

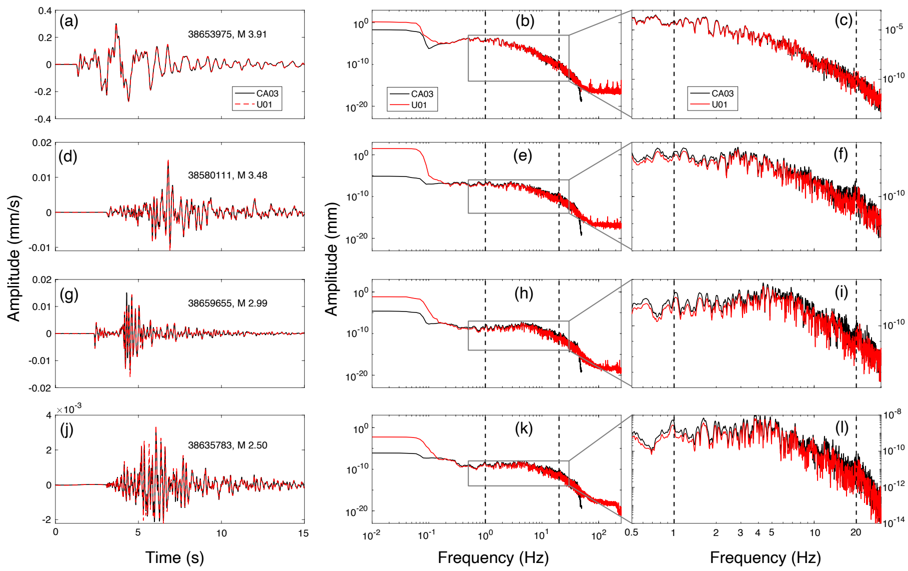

Figure S11. Ground motion comparison of two collocated seismographs. (a) Vertical-component velocity-waveforms of a M 3.9 earthquake at the nodal station U01 and the broadband station CA03. The earthquake event ID is 38653975 (35.63717°/ − 117.47417°/1.6 km). (b) Velocity spectra of the raw waveforms of the M 3.9 event at the collocated stations. The instrumental responses are removed. (c) A zoomed-in view of the gray box in (b). (d) to (l) The waveform and spectrum comparisons for a M 3.5 earthquake (ID: 38580111, 35.59900°/ − 117.37100°/5.7 km), a M 3.0 earthquake (ID: 38659655, 35.68417°/ − 117.52483°/9.2 km), and a M 2.5 earthquake (ID: 38635783, 35.59617°/ − 117.43250°/6.4 km). The waveforms are band-pass filtered at 0.2 to 45.0 Hz with a causal 2nd-order Butterworth filter. The event IDs and locations are from the SCEDC catalog (Hutton et al., 2010).